THE PLANT CELL

The versatility of plant organic acid metabolism in leaves is underpinned by mitochondrial malate–citrate exchange

Chun Pong Lee [ID],[1] Marlene Elsässer,[2] Philippe Fuchs [ID] [2,3] Ricarda Fenske [ID],[1] Markus Schwarzländer[2] and A. Harvey Millar [ID] [1,†*]

1   ARC Centre of Excellence in Plant Energy Biology, University of Western Australia, Crawley 6009, Western Australia, Australia
2   Institute of Plant Biology and Biotechnology, University of Münster, Schlossplatz 8, D-48143 Münster, Germany
3   Institute of Crop Science and Resource Conservation, Rheinische Friedrich-Wilhelms-Universität Bonn, Friedrich-Ebert-Allee 144, D-53113 Bonn, Germany

*Author for correspondence: harvey.milllar@uwa.edu.au
†Senior author.

CPL performed most of the experiments in this manuscript and undertook data analysis. ME and PF conducted experiments with Peredox-mCherry lines and carried out data analysis. RF undertook MRM development and analysis. CPL, MS and AHM developed the experimental plan. CPL and AHM wrote the manuscript and all authors revised the manuscript.

The author responsible for distribution of materials integral to the findings presented in this article in accordance with the policy described in the Instructions for Authors (https://academic.oup.com/plcell) is: A. Harvey Millar (harvey.milllar@uwa.edu.au).

Abstract

Malate and citrate underpin the characteristic flexibility of central plant metabolism by linking mitochondrial respiratory metabolism with cytosolic biosynthetic pathways. However, the identity of mitochondrial carrier proteins that influence both processes has remained elusive. Here we show by a systems approach that DICARBOXYLATE CARRIER 2 (DIC2) facilitates mitochondrial malate–citrate exchange in vivo in *Arabidopsis thaliana*. DIC2 knockout (*dic2-1*) retards growth of vegetative tissues. In vitro and in organello analyses demonstrate that DIC2 preferentially imports malate against citrate export, which is consistent with altered malate and citrate utilization in response to prolonged darkness of *dic2-1* plants or a sudden shift to darkness of *dic2-1* leaves. Furthermore, isotopic glucose tracing reveals a reduced flux towards citrate in *dic2-1*, which results in a metabolic diversion towards amino acid synthesis. These observations reveal the physiological function of DIC2 in mediating the flow of malate and citrate between the mitochondrial matrix and other cell compartments.

Open Access

IN A NUTSHELL

Background: Plants fix CO_2 into organic molecules primarily through photosynthesis, with malate and citrate as the two major stored pools of fixed carbon during the daytime. At night, malate is transported into mitochondria to sustain the tricarboxylic acid cycle and ATP production via oxidative phosphorylation. Citrate can be taken up by mitochondria, but *in silico* flux models suggest that the bulk of mitochondrial citrate is preferentially exported to the vacuole for storage until needed during the day. Although the mitochondrial enzymes controlling malate and citrate metabolism are characterised, the components responsible for mitochondrial malate import and/or citrate export remain enigmatic. Identifying these transport components and their kinetic characters will give new insight into the regulation of day-night fluctuation in malate and citrate metabolism.

Question: Amongst the several likely dicarboxylate carriers (DIC) in Arabidopsis mitochondria, is DIC2 involved in mitochondrial malate transport *in vivo* and what is the specificity of DIC2 function? Is DIC2 dispensable, given that plant metabolism is highly flexible?

Findings: We verified from four independent sources of evidence that DIC2 facilitates malate uptake and citrate export by mitochondria. The loss of DIC2 in the *dic2-1* mutant caused slower vegetative growth, did not change photosynthetic metabolism, but mitochondria isolated from *dic2-1* accumulated citrate inside rather than exporting it. DIC2 absence caused metabolic rearrangements and increases in respiration rate, sugar depletion and peroxisomal citrate metabolism at night in order to compensate for the reduction of mitochondrial citrate availability. DIC2 was essential in maintaining metabolic homeostasis when plants were shifted suddenly from light to dark. Finally, DIC2 expressed in yeast microsomal membranes efficiently and specifically exchanged malate and citrate. Our results revealed that DIC2 function is needed for maintaining malate and citrate-driven metabolic homeostasis, but other carriers also exist that singly or cooperatively carry out similar functions.

Next steps: We will use a similar approach to identify other mitochondrial organic acid transporters, inside and outside of the DIC family. We will then expand such analysis to other classes of mitochondrial carriers, with a goal of building a better metabolic model of plant mitochondria and how they participate in cellular metabolism.

Introduction

Malate is a prominent metabolite that occupies a pivotal node in the regulation of plant carbon metabolism. It is the mainstay of leaf respiration and metabolic redox shuttling between organelles (Scheibe, 2004). Early studies with isolated plant mitochondria demonstrated that exogenous malate can be translocated in exchange for an inorganic phosphate by an unknown butylmalonate-sensitive carrier into the mitochondrial matrix where it is then rapidly oxidized by both mitochondrial malate dehydrogenase (mMDH) and NAD-dependent malic enzyme (NAD-ME), generating oxaloacetate (OAA) and pyruvate as products (Figure 1; Macrae, 1971a, 1971b; Douce et al., 1973; Hatch and Kagawa, 1974; Wiskich, 1974, 1975; Day and Hanson, 1977a). OAA and the product of pyruvate, acetyl-CoA, can then be combined in the first step of the tricarboxylic acid (TCA) cycle to form citrate inside the mitochondrial matrix. However, a combination of enzyme kinetics (Kearney et al., 1972; Journet et al., 1981) and redox coupling reactions in the cytosol and mitochondria (Day and Hanson, 1977b; Wiskich and Day, 1982; Lance and Rustin, 1984) results in marked differences in the rate of malate oxidation and citrate production inside leaf mitochondria in the light and the dark. TCA cycle-driven respiration is largely inhibited in the light and mMDH generally operates in the direction of malate synthesis to facilitate redox coupling between the matrix and other cell compartments, resulting in net mitochondrial OAA import and malate efflux (Tcherkez et al., 2005, 2009; de Oliveira Dal'Molin et al., 2010; Bykova et al., 2014; Hüdig et al., 2015). At night, the requirement for exchanging reducing equivalents between mitochondria and chloroplasts via a malate valve (Kromer, 1995; Raghavendra and Padmasree, 2003; Scheibe, 2004; Selinski and Scheibe, 2019; Zhao et al., 2020) is believed to be minimal due the cessation of both photorespiration and photoinhibitory conditions. The mitochondrial NAD-ME activity and its transcript abundance are highest in the dark (Tronconi et al., 2008); therefore, the synthesis and oxidation of malate is expected to be carried out by both mMDH and NAD-ME to support the synthesis of both citrate and ATP (Lee and Millar, 2016). These metabolic conditions would enable maximal citrate oxidation in the mitochondrial matrix (Igamberdiev et al., 2001; Tovar-Méndez et al., 2003), with excess citrate being exported for storage in the vacuole (Cheung et al., 2014). Mitochondrial citrate is also a major source of cytosolic acetyl-CoA (Schwender et al., 2006; Cheung et al., 2014) required for the elongation of fatty acids and the biosynthesis of isoprenoids and flavonoids (Fatland et al., 2002, 2005; Baud et al., 2003; Oliver et al., 2009). Exported citrate can also be metabolized by aconitase to sustain the TCA cycle and the glyoxylate cycle, as well as to support nitrogen assimilation by producing glutamate or glutamine as an end-product (Carrari et al., 2003; Gauthier et al., 2010; Foyer et al., 2011; Hooks et al., 2014).

Inhibition in the synthesis of citrate from malate-derived OAA in mitochondria and its export leads to floral sterility in potato (*Solanum tuberosum*) plants (Landschütze et al., 1995) and a change in nitrogen incorporation into amino
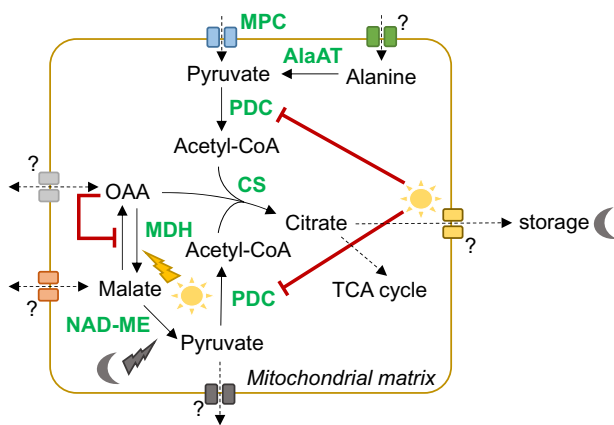
Figure 1 Regulation of malate oxidation leading to citrate production in Arabidopsis. Two malate-oxidizing pathways contribute to the formation of citrate in plant mitochondria. Malate can be oxidized into either OAA or pyruvate. OAA accumulation leads to the inhibition of the malate-oxidizing malate dehydrogenase reaction. The availability of acetyl-CoA for condensation with OAA by citrate synthase is another factor for the regulation of mitochondria malate oxidation. During the day, pyruvate-derived acetyl-CoA amount is limited due to the inhibition of pyruvate dehydrogenase phosphorylation and the reverse reaction of malate dehydrogenase is favored to support photorespiration. At night, NAD-dependent malic enzyme (NAD-ME) and dephosphorylated pyruvate dehydrogenase are activated, allowing optimal supply of acetyl-CoA and OAA for efficient citrate synthesis. While the identity of plant mitochondrial pyruvate carrier (MPC) has recently been confirmed (Le et al., 2021a), the exact molecular identity and in vivo function for malate, OAA, citrate and alanine transporters are not clear. AlaAT, alanine aminotransferase; CS, citrate synthase; MDH, malate dehydrogenase; MPC, mitochondrial pyruvate carrier; PDC, pyruvate dehydrogenase complex.

acids and metabolism in tomato (*Solanum lycopersicum*) leaves (Sienkiewicz-Porzucek et al., 2008). Defects in controlling mitochondrial malate use cause different phenotypic changes and metabolic remodeling: the absence of mMDH activity in Arabidopsis results in a slow growth phenotype and an elevated leaf respiration rate (Tomaz et al., 2010), and the loss of NAD-ME in Arabidopsis causes a significant diversion of excess malate to amino acid synthesis at night (Tronconi et al., 2008). Even though the mitochondrial transport of malate and citrate is clearly at the heart of the remarkable diurnal metabolic flexibility of plants, the identity of components that influence transport rate in vivo has remained elusive.

By identifying homologues of yeast and mammalian carriers in *Arabidopsis thaliana*, several possible candidates that may contribute to mitochondrial malate transport in plants were identified (Picault et al., 2002; Palmieri et al., 2008; Monné et al., 2018). In contrast to the historical, well-established models that mitochondrial metabolite transporters are discrete and highly specific (Wiskich, 1977; Klingenberg, 1979; LaNoue and Schoolwerth, 1979), these carriers appeared to lack substrate specificities under in vitro conditions—for example, dicarboxylate carrier (DIC) isoforms in proteoliposomes can rapidly exchange sulfate with phosphate, malate, OAA, and succinate, with an apparent

low exchange activity in the presence of citrate, 2-oxoglutarate and fumarate (Palmieri et al., 2008). Although in vitro studies have been instrumental in revealing what transport activities can be mediated by a protein, they have limitations that turn out to be critical in the case of plant mitochondrial organic acid transporters. For instance, they cannot suitably consider the often unknown but clearly highly changeable metabolite pool sizes and fluxes that the transporters face in vivo. Reconstitution with a specific orientation of the transporter is not possible in most in vitro systems, but is critical for substrate specificity and respiratory physiology in vivo. Further, the specific local lipid environment and the pronounced electrochemical gradients ($\Delta\psi$, ΔpH), both of which are likely to be central for inner mitochondrial membrane transport activity and specificity (Lee and Millar, 2016), can only be roughly considered. If we are to understand the roles that metabolite transporters fulfill in the living plant, additional information is needed about the influence of an individual transporter on net transport across a membrane within a physiologically meaningful context. Yet, in planta studies of mitochondrial metabolite transporter proteins that address the question of their in vivo influence on metabolism, requiring a systems perspective to consider their integration in the metabolic network, have been lacking.

In this study, we determine that DIC2 functions as a high affinity malate–citrate antiporter in Arabidopsis mitochondria, through evidence from the reverse genetic approach in combination with comprehensive in vitro, in organello, and in vivo analyses. We present strong evidence that plant DIC2 activity plays a critical role in dynamically coordinating anaplerotic metabolism with assimilatory and catabolic pathways between the mitochondria and other cellular compartments.

Results

DIC2 mutation causes decelerated vegetative growth rate that cannot be compensated by other mitochondrial dicarboxylate carrier isoforms

DIC2 is a mitochondrial protein based on interpretation of fluorescent microscopy images of transient (Van Aken et al., 2009) or stable expression of DIC2-GFP (Supplemental Figure S1) and Arabidopsis mitochondrial proteome analysis by mass spectrometry (Senkler et al., 2017; Fuchs et al., 2020). Three T-DNA insertion lines were obtained in order to study the possible physiological and metabolic consequences of a defect in DIC2 (At4g24570) function in planta. Only the homozygous *dic2-1* line has a T-DNA insertion within the open reading frame of *DIC2*, resulting in the complete loss of *DIC2* transcript (Figure 2A; Supplemental Figure S2A). Using selective reaction monitoring mass spectrometry to determine protein abundance (Taylor et al., 2014), we found that two different DIC2 peptides, detectable in Col-0, were not detectable in mitochondria isolated from *dic2-1* plants (Figure 2A; Supplemental Figure S2B), confirming *dic2-1* as a null mutant for DIC2. The homozygous *dic2-1*
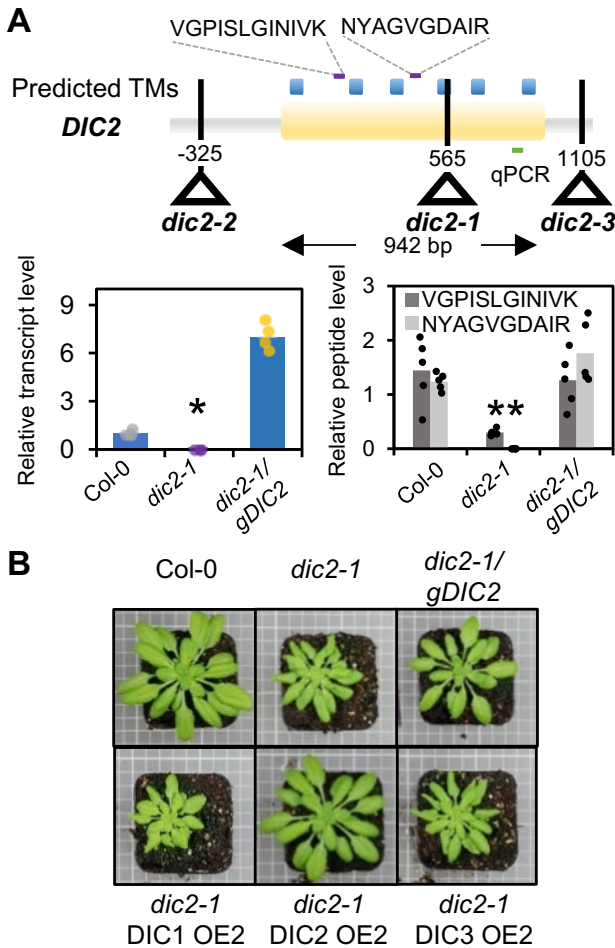
Figure 2 Phenotypic characterization of the *DIC2* mutant. A, Top, gene model of DIC2 showing predicted transmembrane domains based on ARAMEMNON consensus prediction (Schwacke et al., 2003), the position of T-DNA insertion in the *dic2-1* line and locations of peptides for selective reaction monitoring mass spectrometry (in purple lines) and the transcript for qPCR (in green line). Bottom left, expression levels of *DIC2* as determined by qPCR in different genotypes ($n = 4$). Bottom right, abundance analysis of unique peptides of DIC2 using the quantifier ion transitions VGPISLGINIVK and NYAGVGDAIR ($n = 5$). Individual data points were overlaid in dots in bar graphs. Asterisks denote significant differences between *dic2-1* versus Col-0 and *dic2-1* versus *dic2-1/gDIC2* based on ANOVA and post hoc analysis (*$P < 0.05$). B, Vegetative phenotype of Col-0, *dic2-1* and complemented lines (*gDIC2*, native promoter; *OE*, 35S promoter) grown on soil under short-day conditions (8-h light/16-h dark) for 49 days after germination. Representative top view of various genotypes is shown. Expression levels are shown in Supplemental Table S1.

showed reduced root growth during seedling development (Supplemental Figure S2C) and a significantly decreased rate of rosette expansion (Figure 2B; Supplemental Figure S2, D and E). From Day 42, the number of leaves emerged from Col-0 and *dic2-1* was identical, but the mutant leaves were smaller and curly with a more rugose surface (Supplemental Figure S2F). *dic2-1* could not reach the full rosette diameter of Col-0 after 1 week of bolting (Supplemental Figure S2G). *dic2-1*-specific phenotypes could be observed regardless of the photoperiod (Supplemental Figure S2H). These

phenotypes could be restored by introducing *DIC2* under the control of its native promoter (*dic2-1/gDIC2*) or a cauliflower mosaic virus 35S promoter (*dic2-1/DIC2 OE*; Figure 2B; Supplemental Figure S2D). We attempted to rescue the *dic2-1* phenotype by expressing *DIC1* and *DIC3* in the *dic2-1* background (*dic2-1/DIC1 OE* and *dic2-1/DIC3 OE*, respectively), but neither could complement the loss of DIC2, not even partially (Figure 2B). These results indicate that DIC2 does not share substrate preferences and/or specificities with DIC1 or DIC3 in planta.

Net citrate export by energized mitochondria is compromised as a consequence of DIC2 loss

To explore the transport function of DIC2, we first tested the hypothesis that malate is the main substrate for DIC2 in the context of intact isolated mitochondria, as inferred previously by a proteoliposome-based approach (Palmieri et al., 2008). To this end, we monitored the transport activity for ^{14}C-malate by nonenergized isolated mitochondria in a minimal reaction medium that lacked added cofactors and ADP to allow malate to more slowly accumulate while preventing its conversion into other TCA cycle intermediates. Under such conditions, the initial uptake rate of 200-μM [^{14}C]-malate into mitochondria of *dic2-1* was three-fold lower compared to Col-0 and *dic2-1/gDIC2* (Figure 3A). Hence, DIC2 facilitates a significant malate uptake capacity in isolated Arabidopsis mitochondria and its loss limits this uptake, even in the presence of other potential carriers for malate transport.

Titrations with respiratory substrates at different concentrations revealed no obvious differences in the rate of internal or external NADH-driven O_2 consumption between Col-0 and *dic2-1* (Supplemental Figure S3A). No change in the abundance or activity of electron transport chain (ETC) supercomplexes (Supplemental Figure S3B), the relative abundance of TCA cycle enzymes, pyruvate dehydrogenase or NAD-ME (Supplemental Figure S3C), or their K_m and V_{max} (Supplemental Table S2) were observed when mitochondria isolated from these genotypes were compared. This eliminated the possibility of a clear defect in the ETC or a specific step of the TCA cycle in *dic2-1*; instead, any shift in the distribution of specific metabolites between the matrix and extra-mitochondrial space in the mutant could reasonably be attributed directly to the absence of DIC2 and/or indirectly to the enzymatic regulatory compensation as the result of DIC2 loss.

Isolated mitochondria were then tested for their ability to consume malate under state III respiration condition and to generate and export metabolites synthesized from malate (Figure 3B; Supplemental Figure S4A). The rate of malate uptake by energized mitochondria was similar between the genotypes (Figure 3C), possibly due to compensation by other malate carriers. The abundance of pyruvate, generated through the action of NAD-ME from imported malate, increased linearly over time in mitochondria of Col-0 and *dic2-1/gDIC2*, whereas it leveled off in *dic2-1* (Figure 3D).
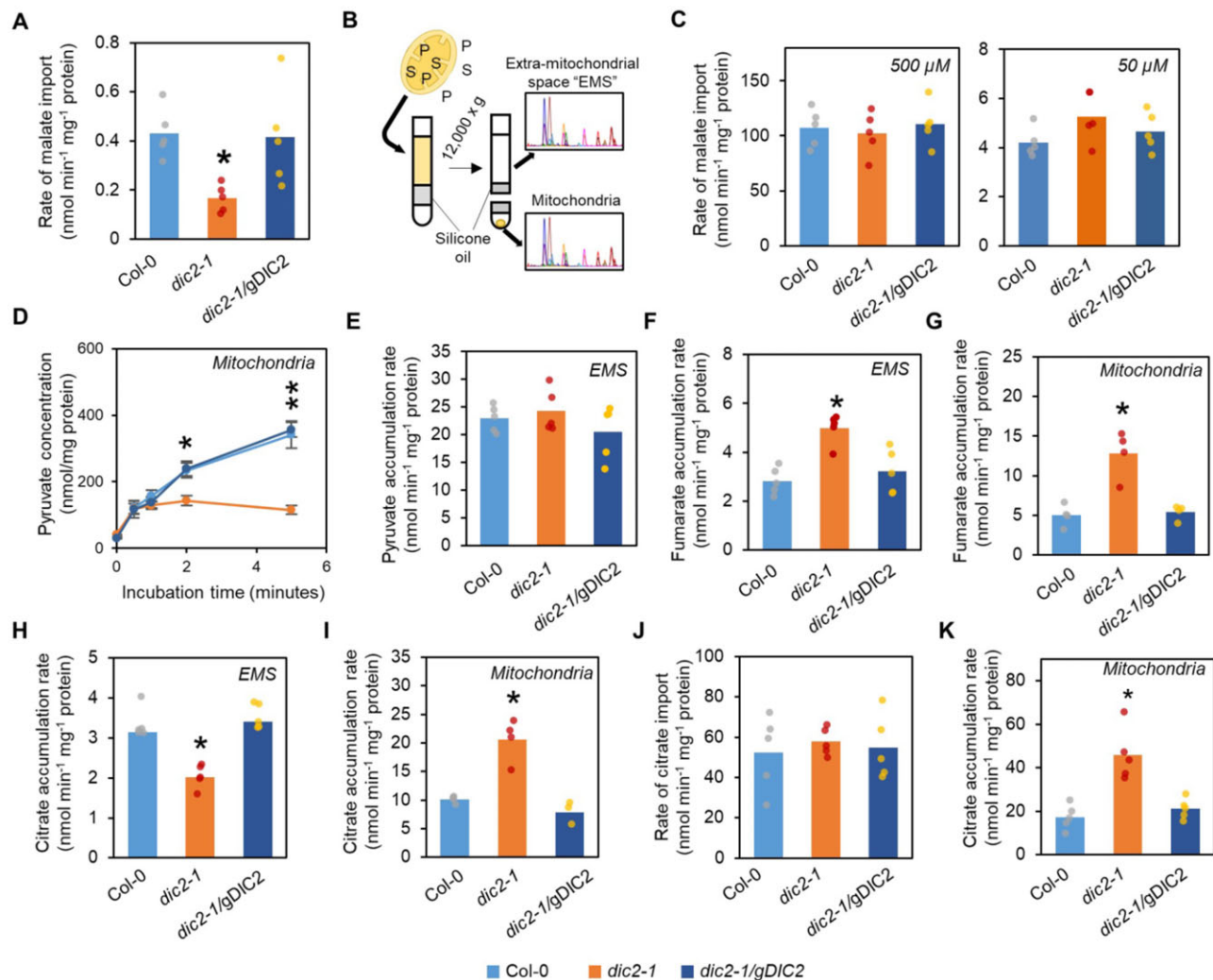
Figure 3 Uptake, consumption and export of malate or citrate by mitochondria isolated from the *DIC2* mutant. A, Uptake rate of 200 μM [^{14}C]-malate into isolated mitochondria under nonenergizing conditions. B, Experimental design for monitoring substrate consumption, product formation and metabolite transport kinetics of isolated mitochondria. Mitochondria are fed with a substrate under energized conditions. After indicated time interval, mitochondria are separated from extra-mitochondrial space by centrifugation through a silicone oil layer. These fractions are collected, and substrates (S) and products (P) in the EMS and in pelleted mitochondria are quantified by selective reaction monitoring mass spectrometry. C, Uptake rate of 500 μM (left) or 50 μM (right) malate into isolated mitochondria under energizing conditions. D, Time-course of pyruvate concentration in mitochondria in the presence of 500-μM external malate. E–I, Bar graphs showing the accumulation rate of (E) pyruvate in the EMS, (F) fumarate in the EMS, (G) fumarate in mitochondria, (H) citrate in the EMS, and (I) citrate in mitochondria upon 500-μM malate feeding. (J) Uptake rate of 500-μM citrate into isolated mitochondria under energizing conditions. K, Citrate accumulation rate in mitochondria when incubated with 500 μM external citrate. All data are presented as mean (± sᴇ) from at least three biological replicates. Individual data points were overlaid in dots in bar graphs. Asterisks denote significant differences between *dic2-1* versus Col-0 and *dic2-1* versus *dic2-1/gDIC2* based on ANOVA and Tukey's post hoc analysis (*$P < 0.05$; **$P < 0.01$). Response curves shown can also be found in Supplemental Figure S4, A and B.

Consistent with this, *dic2-1* mitochondria exhibited a 20%–30% lower V_{max} for malate-dependent state III O$_2$ consumption (Supplemental Figure S4C). However, pyruvate accumulation in the extramitochondrial space (EMS) was maintained in the mutant mitochondria in the same way as in Col-0 (Figure 3E), ruling out the possibility of a defect in pyruvate export. The apparent increases in fumarate export to the EMS and its accumulation in mitochondria appear to be compensatory effects to avoid prolonged overaccumulation of malate through its rapid removal by dehydration in the *dic2-1* matrix (Figure 3, F and G), which would provide

an explanation for the apparent lack of mitochondrial malate accumulation in *dic2-1* compared to controls (Supplemental Figure S4A). These data pinpoint a reduced rate of malate oxidation in the matrix of malate-fed *dic2-1* mitochondria as a plausible cause for the observed decrease in malate-dependent respiration and pyruvate formation.

Strikingly, upon malate feeding, there was a much higher rate of citrate accumulation inside *dic2-1* mitochondria (Figure 3I), accompanied by a lower rate of export of citrate to the EMS when compared to Col-0 mitochondria (Figure 3H). We thus hypothesized that excess citrate in

dic2-1 mitochondria was caused by compromised citrate export, which then prevented OAA condensation in the citrate synthase reaction and thus suppressed mMDH activity (Fahien et al., 1988). To confirm this, we tested the ability of mitochondria to directly consume citrate (Supplemental Figure S4B). Under such conditions, NAD-ME and mMDH activities became inhibited, as demonstrated by the low mitochondrial export rate of pyruvate. There was no change in citrate-dependent O_2 consumption mitochondria from all genotypes (Supplemental Figure S4D), further confirming that the mitochondrial citrate import rate was not affected and the reduction in malate-dependent respiration by *dic2-1* was likely caused by the citrate accumulation in the matrix triggering an OAA inhibition of mMDH. While the uptake rate of citrate by mitochondria was not altered significantly (Figure 3J), the rate of citrate accumulation in *dic2-1* mitochondria was 2.3-fold higher than Col-0 or *dic2-1/gDIC2* (Figure 3K) without compromising product formation and accumulation rates (Supplemental Figure S4B). Taken together, while DIC2 is directly responsible for a portion of malate uptake, its loss also influences the export of citrate. However, the fact that citrate export was not completely abolished by the loss of DIC2 suggests that this critical export across the inner mitochondrial membrane is also not solely dependent on the presence of DIC2.

DIC2 preferentially exchanges malate against citrate in proteoliposomes

Our finding that DIC2 loss alters mitochondrial citrate export was unexpected, since proteoliposome-reconstituted DIC2 has been reported to have a relatively low citrate exchange activity against sulfate (Palmieri et al., 2008). It is possible that, in the absence of an electrochemical gradient across the liposomal membrane, DIC2 does not support an electrogenic exchange of a divalent dicarboxylate/sulfate/phosphate against a trivalent citrate at pH 7.0. To verify whether DIC2 acts as citrate transporter, or its loss rather indirectly contributes to a decrease in citrate export in organello, DIC2 was expressed heterologously in yeast and isolated microsomal membrane fraction was reconstituted into proteoliposomes (Figure 4A; Supplemental Figure S5A). Proteoliposomes preloaded with sulfate, phosphate, or citrate were incubated with TCA cycle organic acids (250 μM each) simultaneously at pH 6.0 (to shift the citrate buffer toward H-citrate^{2-}) to assess DIC2 substrate specificity under a competitive condition. DIC2 did not demonstrate significant transport of any metabolites in the presence of internal sulfate or phosphate, including malate, succinate and OAA, when compared to the empty vector control (Supplemental Figure S5, B and C). In contrast, DIC2 showed a clear preference for malate when proteoliposomes were preloaded with citrate (Figure 4B). Malate–citrate exchange by DIC2 was saturable in a time- and concentration-dependent manner (Figure 4C; Supplemental Figure S5D), with an apparent K_m of 48 μM for malate (Figure 4D) which is 10-fold lower than in a previous report (0.51 mM; Palmieri et al., 2008). While the

concentration of malate and citrate in the intermembrane space is currently unknown, such a K_m value is below their expected cytosolic amount in plants (Gerhardt and Heldt, 1984; Gerhardt et al., 1987; Winter et al., 1994) and within the expected concentration range of most organic acids in intact mammalian mitochondria (10–50 μM; Chen et al., 2016). Our results also indicate that citrate is transported by DIC2 as a divalent anion or a trivalent form with cotransport of a proton. Together with the data from isolated mitochondrial assays, we concluded that DIC2 is a biologically relevant high affinity and directional malate$_{in}$/citrate$_{out}$ transporter.

DIC2 function affects leaf dark respiration by modulating NAD homeostasis

We then set out to determine how defects in mitochondrial malate import and citrate export operate in planta and if they could explain the observed phenotypes of *dic2-1*. In total we investigated three scenarios where leaf mitochondria operate under different flux modes: in the light, during the transition from light to dark and in the dark. First, we carried out chlorophyll fluorescence and infrared gas-exchange analyses at different light intensities, as changes in photosynthetic performance can cause many metabolic perturbations and mask other primary metabolic effects in mutants. There was no change in the CO_2 assimilation rate (Figure 5A), stomatal conductance, transpiration rate, photosynthetic electron transport rate, photosystem II quantum yield, or nonphotochemical quenching in *dic2-1* leaves (Supplemental Figure S6, A–E). When plants were shifted to high light for 3 and 16 h, we did not detect any changes in the maximum photochemical efficiency of PSII (F_v/F_m) among *dic2-1*, Col-0, and *dic2-1/gDIC2* (Supplemental Figure S6F). These results indicated that the loss of DIC2 has no direct impact on photosynthetic performance.

Second, we examined the transition from light to darkness where leaf mitochondria undergo several rapid changes in metabolic activity as photorespiration ceases and the noncyclic mode of the mitochondrial TCA cycle is activated. Upon transfer of illuminated leaves to darkness, *dic2-1* exhibited a more rapid release of CO_2 in the first 30–40 s before reaching a higher rate of steady-state respiratory CO_2 release compared to Col-0 and *dic2-1/gDIC2* (Figure 5B). The sharp CO_2 release upon sudden darkness is indicative of a post-illumination burst (PIB) of respiration, an estimate of the degree of respiratory glycine oxidation (Rawsthorne and Hylton, 1991). To examine if photorespiratory activities were altered in the mutant, we grew the mutant under high CO_2 (0.2%) to suppress photorespiration but no rescue of the phenotype was achieved (Supplemental Figure S6G). These data indicate that an altered photorespiratory activity after dark shift is not the primary cause for the change in PIB response by *dic2-1*. Since malate/OAA utilization in mitochondria can control the degree of glycine oxidation by regulating NADH/NAD$^+$ (e.g. via a malate shuttle; Journet et al., 1981), we hypothesized that a PIB increase in *dic2-1* could be linked to an altered distribution of TCA cycle metabolites between mitochondria and cytosol (and possibly
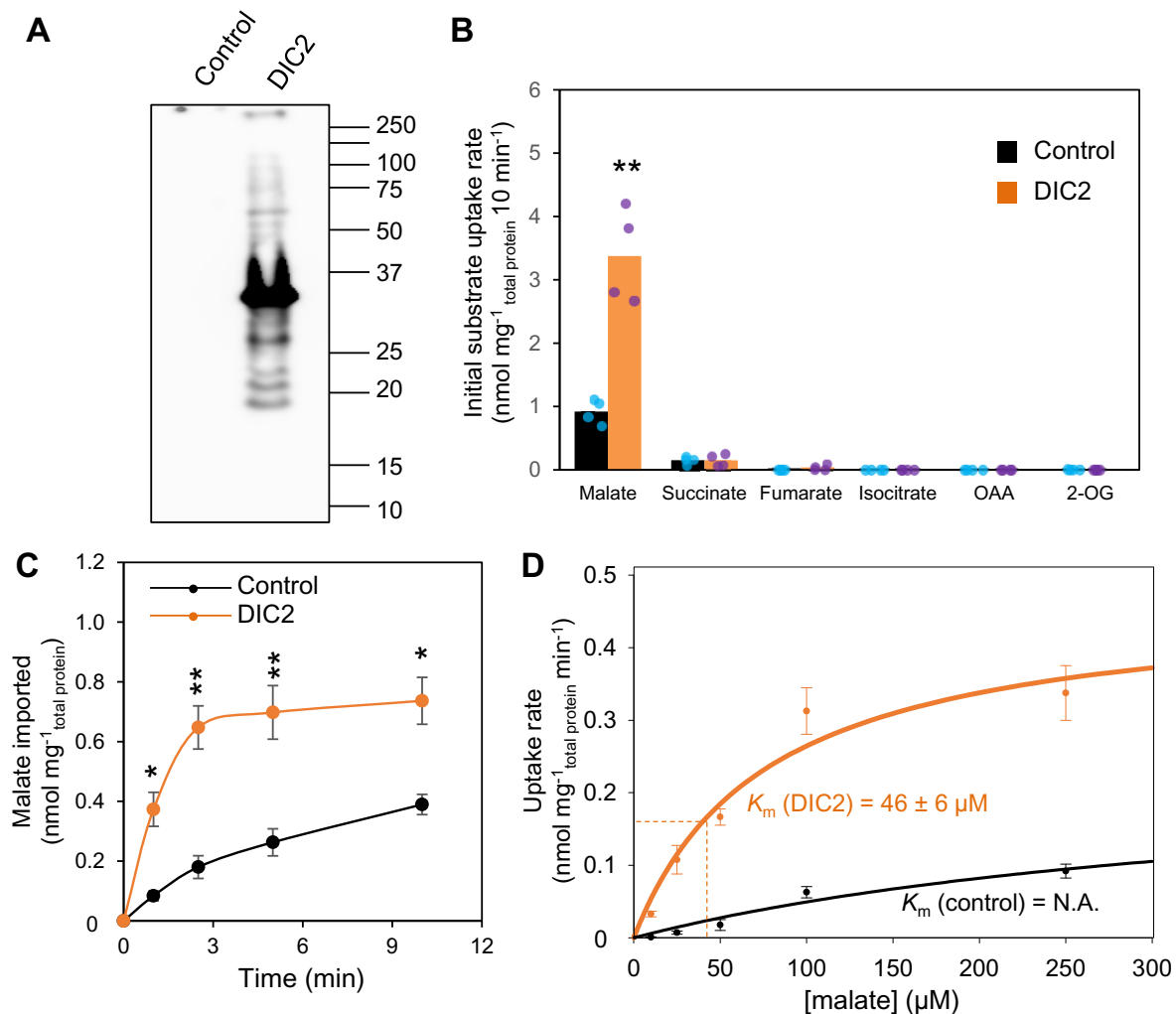
Figure 4 Kinetic analysis of DIC2 substrate specificity by proteoliposome transport assay. A, Proteoliposomes reconstituted with microsomal membrane expressing V5-tagged empty vector control or DIC2 were analyzed by immunoblotting with anti-V5 tag antibodies. Image shown was exposed for 1 min. Gel loading control and images obtained from other exposure times are shown in Supplemental Figure S5A. B, Quantification of transport of TCA cycle organic acids (100 μM each) into proteoliposomes preloaded with 10-mM citrate. ** indicate a significant difference between empty vector and DIC2 with $P < 0.01$ according to the Student's t test. Individual data points were overlaid in dots. C, Time course of malate uptake (100 μM) into 10-mM citrate-loaded proteoliposomes containing DIC2. Asterisks indicate a significant difference between empty vector and DIC2 according to the Student's t test (**$P < 0.01$ and * < 0.05). D, Kinetic characteristics of DIC2 reconstituted into 10-mM citrate-loaded proteoliposomes in the presence of varying external malate concentrations (0–250 μM). Data are expressed as mean ± SE from four independent experiments.

plastids), leading to changes in metabolic and/or NAD redox state in these compartments. To capture any rapid and transient changes in NAD redox state during a sudden dark shift, we utilized a fluorescent protein biosensor Peredox-mCherry which reports cytosolic $NADH/NAD^+$ through the ratio of tSapphire to mCherry fluorescence ($\log_{10}(tS/mC)$), where a higher $\log_{10}(tS/mC)$ corresponds to a more reduced NAD pool (Steinbeck et al., 2020). We observed equally high $NADH/NAD^+$ ratios in Col-0 and *dic2-1* plants during illumination (Figure 5C). However, upon transfer to darkness, the expected decline in $NADH/NAD^+$ ratios in the first 100 s was significantly slower in *dic2-1* compared to Col-0. Both differences in PIB and NAD redox status upon rapid transition to darkness indicate some defect in switching between light and dark flux modes by *dic2-1* mitochondria.

Third, we examined metabolic changes to *dic2-1* leaves during the night. DIC2 expression steadily increased over the course of nighttime, followed by a decline from the peak at the end of dark photoperiod to the lowest level in the light (Supplemental Figure S6H). Intriguingly, while there was no difference in the $NADH/NAD^+$ ratio between the two genotypes over the course of the dark–light cycle (Figure 5D), the leaf nighttime respiration rate (R_N) remained consistently higher in the mutant (Figure 5E). Given that primary metabolites are crucial determinants for regulating transcript abundance during a diurnal cycle (Gibon et al., 2006), there appears to be a metabolic rearrangement in the mutant to avoid any detrimental impact of DIC2 absence on NAD redox equilibrium, albeit at the expense of heightened respiration (Figure 5, B and E) and slower vegetative growth
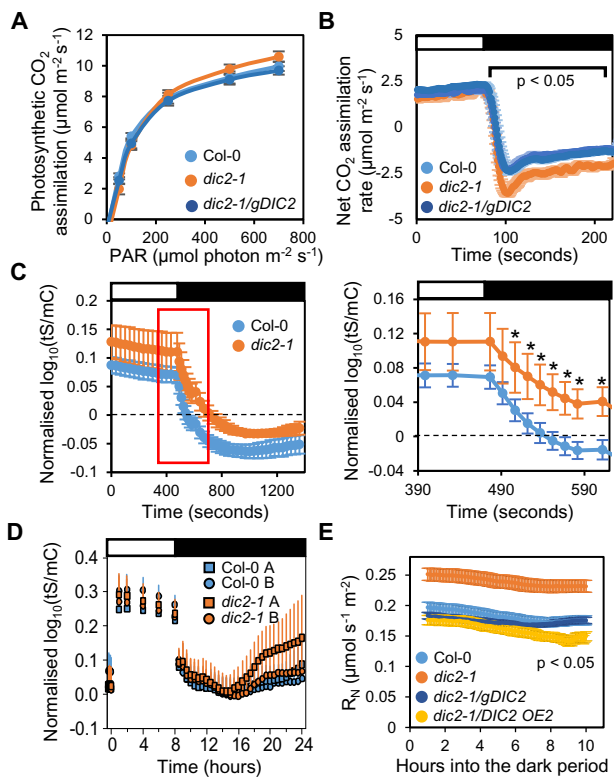
Figure 5 Photosynthetic and respiratory phenotypes of the DIC2 knock-out mutant. A, Photosynthetic CO_2 assimilation rate at different PAR with CO_2 concentration at 400 ppm and temperature at 22°C ($n = 7$, mean ± SE, no significant difference based on one-way ANOVA). B, Determination of post-illumination CO_2 burst. A single leaf illuminated with actinic light of 1,000 μmol m^{-2} s^{-1}, CO_2 concentration of 100 ppm at 25°C was darkened for 2 min and post-illumination burst was monitored in the first 30 s ($n = 6$, mean ± SE, data points within the bracket indicate significant differences of $P < 0.05$ for dic2-1 versus Col-0 and dic2-1 versus dic2-1/gDIC2 comparisons based on one-way ANOVA with Tukey post hoc test). C, Cytosolic NAD redox dynamics of the leaves of 6-week-old plants in response to a sudden light-to-dark transition. Redox changes of the NAD pool correspond to the Peredox-mCherry ratio ($\log_{10}$(tS/mC)), i.e. high ratio indicates high NADH/NAD$^+$ ratio. Dark adapted leaf discs were illuminated at actinic light of 220 μmol m^{-2} s^{-1} before they were transferred to the dark. The 5-min light/15-min dark time course is shown on the left, with the red rectangle indicating the moment when significant differences in NAD redox state were observed. Zoom-in of this red rectangle time interval is shown on the right. Each data point represents mean ± SD ($n \geq 6$), with asterisks indicating a significant difference with $P < 0.001$ based on multiple t tests (alpha = 5%) from the Holm–Sidak Method. D, Changes in the cytosolic NAD redox state over 8-h light/16-h dark diurnal cycle. Leaf discs were exposed to actinic light of 120 μmol m^{-2} s^{-1} before light was switched off. Two independent lines (A and B) for each genotype were measured. Data shown indicate mean ± SD ($n \geq 8$) with no significant differences found between lines. E, Time course of leaf respiration measurements in the dark (R_N) as measured by Q2 ($n > 8$, mean ± SE, all time points for the dic2-1 line are significantly different from other genotypes with $P < 0.05$ based on one-way ANOVA with Tukey post hoc test).

(Figure 2B). Taken together, DIC2 activity may have a greater influence on metabolism and mitochondrial respiration in the dark, most likely through modulating TCA cycle reactions in the cytosol and/or mitochondria to maintain metabolic homeostasis required for fundamental cellular functions.

2-oxoglutarate sharply accumulates in dic2-1 leaves upon shift to darkness

To gain further insight into how DIC2 function is integrated into metabolism and influences NAD redox state in vivo, we carried out metabolite profiling of leaf samples collected from 6-week-old plants at different time points of a diurnal cycle (Figure 6A; Supplemental Figure S7A). The metabolite profiles of malate, fumarate, and succinate over a diurnal cycle were generally similar between genotypes. Also, a similar pattern in daytime glycine and serine accumulation was observed, despite a clear difference in PIB (Figure 5B), further confirming that DIC2 function does not directly affect photorespiratory flux. The most notable metabolite level changes in dic2-1 plants compared to Col-0 and dic2-1/gDIC2 were observed in the first hour after the sudden shift to darkness, including two- to four-fold higher abundances of pyruvate, citrate, and isocitrate, and a remarkable 10-fold increase in 2-oxoglutarate abundance (2-OG). Several amino acids linked to 2-OG utilization also changed in abundance in dic2-1. In particular, the glutamate pool in dic2-1 was larger than in Col-0 and dic2-1/gDIC2 plants 1 h after the dark shift and during the light photoperiod, while GABA and glutamine abundances remained unchanged. Aspartate and alanine, which can be converted into OAA and pyruvate respectively in a reversible reaction that requires glutamate/2-OG transamination, were also more abundant in dic2-1 after 1 h of darkness, while aspartate-derived threonine accumulated in the mutant throughout the diurnal cycle. Branched chain amino acids (BCAAs), which use 2-OG as co-substrate to initiate their catabolism in mitochondria (Hildebrandt et al., 2015), were generally higher in abundances in dic2-1 plants at night. Such increases in cellular 2-OG utilization in dic2-1 would be consistent with increases in citrate retention and subsequent 2-OG and/or glutamate formation and export by mutant mitochondria (Figure 3I). Overall, the metabolite profiles revealed that the loss of DIC2 function causes an altered 2-OG metabolism in the dark, which may provide a metabolite buffer to compensate for a defect in mitochondrial DIC2 activity while cytosolic NAD redox state is maintained.

We next further investigated the cause of the increased R_N in dic2-1. An increased nighttime consumption rate of sucrose, but not of glucose or fructose, by dic2-1 was observed (Figure 6B; Supplemental Figure S7B). The expression of several nutrient-responsive senescence markers, SAG101 (He and Gan, 2002), WRKY53 (Miao and Zentgraf, 2007), and SEN1 (Oh et al., 1996), was also highly upregulated in the mutant in the dark but not in the light (Supplemental Figure S7C), suggesting nighttime starvation. These results, combined with a lack of photosynthetic differences (Figure 5A; Supplemental Figure S6, A–E), suggest that an accelerated depletion rate of carbon stores via respiration leads to nighttime starvation in dic2-1. Thus, changes in

metabolite abundances noted above were accompanied by a higher sucrose catabolism in the mutant at night. When leaf discs were incubated in the dark with uniformly labeled ^{14}C-malate or ^{14}C-leucine, we found that *dic2-1* showed higher $^{14}CO_2$ emissions than Col-0 and *dic2-1/gDIC2* from malate (Figure 6C) but not leucine (Supplemental Figure S7D). The observed increase in BCAAs accumulation in *dic2-1* in the dark (Figure 4A) may thus be contributed by increased TCA cycle fluxes into biosynthetic pathways and/or an elevated proteolysis, while BCAAs breakdown for respiration remained unchanged. Thus, these data indicated that the loss of DIC2 results in increased sucrose utilization (or export for use by other tissues) and TCA cycle-facilitated respiration to compensate for a failure to maintain the homeostasis of organic acid oxidation.

A defect in organic acid use causes accelerated leaf senescence of the DIC2 knockout during prolonged darkness

To further examine the extent to which DIC2 transport function influences whole plant sugar-sensitive organic acid use, we subjected Arabidopsis plants to darkness for 15 days. The mutant exhibited an accelerated decline in F_v/F_m beginning around 7 days of darkness (Supplemental Figure S8A). Leaves of *dic2-1* were more yellowed compared with the Col-0 and the *dic2-1/gDIC2* after 10 days (Figure 6D; Supplemental Figure S8B). When 15 days dark-treated plants were transferred back to the normal short-day cycle, only Col-0 and *dic2-1/gDIC2* could recover after 7 days. To identify the TCA cycle metabolites that were affected the most by the absence of DIC2, we carried out a time-course measurement of organic acid contents over 12 days of prolonged darkness (Figure 6E; Supplemental Figure S8C). When F_v/F_m began to decline more rapidly in *dic2-1* on Day 7 (Supplemental Figure S8A), only malate, 2-OG, and citrate were significantly more accumulated. While all TCA cycle intermediates were significantly increased in the mutant 10 days after dark treatment, malate and 2-OG accumulated at least 10 times higher in abundance in the mutant than Col-0 and *dic2-1/gDIC2*. Citrate abundance in the Col-0 and *dic2-1/gDIC2* progressively declined from Days 3 to 12 of darkness, whereas it remained unchanged in *dic2-1* plants throughout the treatment. Notably, the accumulation of these metabolites by *dic2-1* in planta would be consistent with a failure to properly regulate mitochondrial malate and citrate metabolism. Throughout a diurnal cycle, pool sizes of these metabolites were unchanged; it was only when plants were exposed to dark-induced starvation that altered patterns in the utilization of specific organic acids manifested (Figure 6A).

DIC2 modulates metabolite turnover through TCA cycle and amino acid metabolism, which supports citrate export at night

The observed decrease in malate-dependent O_2 consumption by isolated mitochondria (Supplemental Figure S4C)

did not explain the faster dark respiration of intact leaves (Figures 5, E and 6, C). This could be due to the absence of any extramitochondrial metabolism, which in vivo maintains metabolite supply for sustaining mitochondrial transport activities, TCA cycle and respiration in response to rearranged metabolism and transport in the mutant. To account for the apparent homeostasis in metabolite pool sizes (Figure 5A), we postulated that there could be a flux change in certain steps of metabolism to compensate for the reduced malate import and citrate export by *dic2-1* mitochondria.

To determine if *dic2-1* metabolizes carbon differently, we traced the labeling of U-^{13}C-glucose into the TCA cycle and closely related amino acids in leaf discs in the dark for 8 h. The ^{13}C-tracing data were expressed on the basis of per O_2 molecule consumed to take into consideration the observed differences in organic acid use-dependent CO_2 release and dark respiration rate (Supplemental Data Set S1). Consistent with DIC2 function as a mitochondrial citrate exporter, *dic2-1* displayed a decreased rate of citrate labeling over the course of dark incubation (Figure 7A). On the other hand, the citrate pool remained stable in the dark in *dic2-1* (Figure 6A) possibly due to compensation by altered citrate turnover rates in other compartments. A decrease in OAA availability from cytosolic phosphoenolpyruvate (PEP) carboxylase could also be ruled out, since labeling of $m + 3$ aspartate (a proxy for labeled OAA) was not altered (Supplemental Figure S9, A and B). Decreased citrate labeling was accompanied by a significant increase in the abundance of labeled 2-OG due to a higher total pool in the mutant (Figure 7B; Supplemental Data Set S1), which coincided with an increased rate of ^{13}C incorporation into glutamine (Figure 7C). These increases could be facilitated by a higher mitochondrial glutamate efflux rate since there was a higher initial 2-OG accumulation rate in substrate-fed *dic2-1* mitochondria (Supplemental Figure S4, A and B), implying that an enhanced flux into glutamine was necessary to remove excess mitochondrial 2-OG by mitochondrial glutamate transamination reactions in concert with a cytosolic glutamine synthase (Bernard and Habash, 2009). The downstream extra-mitochondrial biosynthetic pathway of aspartate, threonine, and asparagine, were increased in total label abundances in the mutant mainly due to a significantly higher incorporation as $m + 2$ species via the TCA cycle (Figure 7, D and E; Supplemental Figure S9, C–H and Supplemental Data Set S1), while the total amount of succinate, fumarate, and malate labeled via the TCA cycle ($m + 2$) and/or PEP-OAA interconversion ($m + 3$) did not change (Figure 7F; Supplemental Figure S9, I–L). These results are consistent with a metabolic diversion of excess malate that was not consumed by mitochondria for citrate synthesis, export, and storage into aspartate.

The loss of DIC2 causes a significant metabolic rearrangement towards amino acid synthesis with less citrate available from the TCA cycle for storage at night (Supplemental Figure S9M). To further examine if citrate
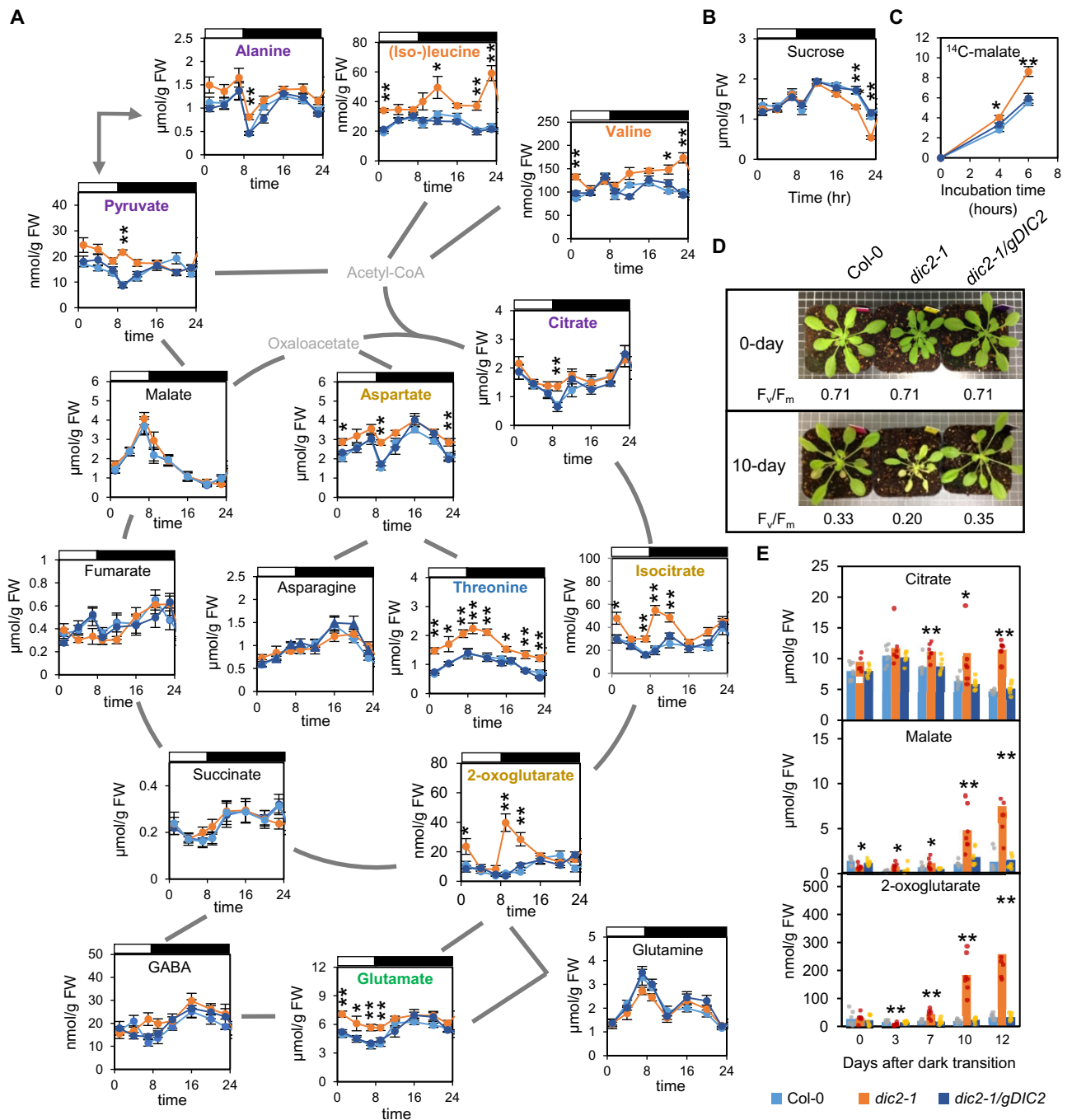
Figure 6 Quantitative analysis of metabolites associated with the TCA cycle in a diurnal cycle and during prolonged darkness in the DIC2 knock-out mutant. A, Plants were grown under short day conditions for 6 weeks and leaf discs were collected at 1, 4, 8, 12, and 15 h after dark shift and 1, 4, and 7 h after light shift. Metabolites in this figure were analyzed by LC–MRM–MS ($n \geqslant 6$). Metabolites are colored according to their accumulation pattern in *dic2-1* in a diurnal cycle: Orange, accumulates at night; Brown, accumulates during light and dark shift; Green, accumulates predominantly during the day; Blue, accumulates throughout a diurnal cycle; Purple, accumulates only after the first hour of dark shift; gray, metabolite not measured. B, Sucrose levels in leaf discs from Col-0, *dic2-1* and *dic2-1/gDIC2* collected at different time points of a diurnal cycle as quantitatively determined by GC–MS against authentic standards ($n \geqslant 6$). C, CO_2 evolution of leaf discs incubated in uniformly labeled ^{14}C-malate. $^{14}CO_2$ was captured in a NaOH trap, radiolabel in leaf discs was extracted and the radioactivity in these samples was counted by a liquid scintillation counter. Data shown are the percentage of CO_2 released relative to the total amount of radiolabel incorporated into leaf metabolism ($n \geqslant 7$). D, Images of 5- to 6-week-old, short-day grown plants treated with 0 and 10 days of extended darkness. Values for maximum quantum efficiency of photosystem II (*Fv/Fm*) are shown below each genotype ($n = 6$). E, Changes in citrate, 2-OG and malate content in Arabidopsis plants after 0, 3, 7, 10, and 12 days of extended darkness treatment ($n \geqslant 6$). Individual data points were overlaid in dots in bar graphs. Each data point represents mean and each error bar represents ± SE where appropriate. Asterisks indicate a significant change for *dic2-1* versus Col-0 and *dic2-1* versus *dic2-1/gDIC2* comparisons as determined by one-way ANOVA with Tukey post hoc test (*$P < 0.05$; **$P < 0.01$).
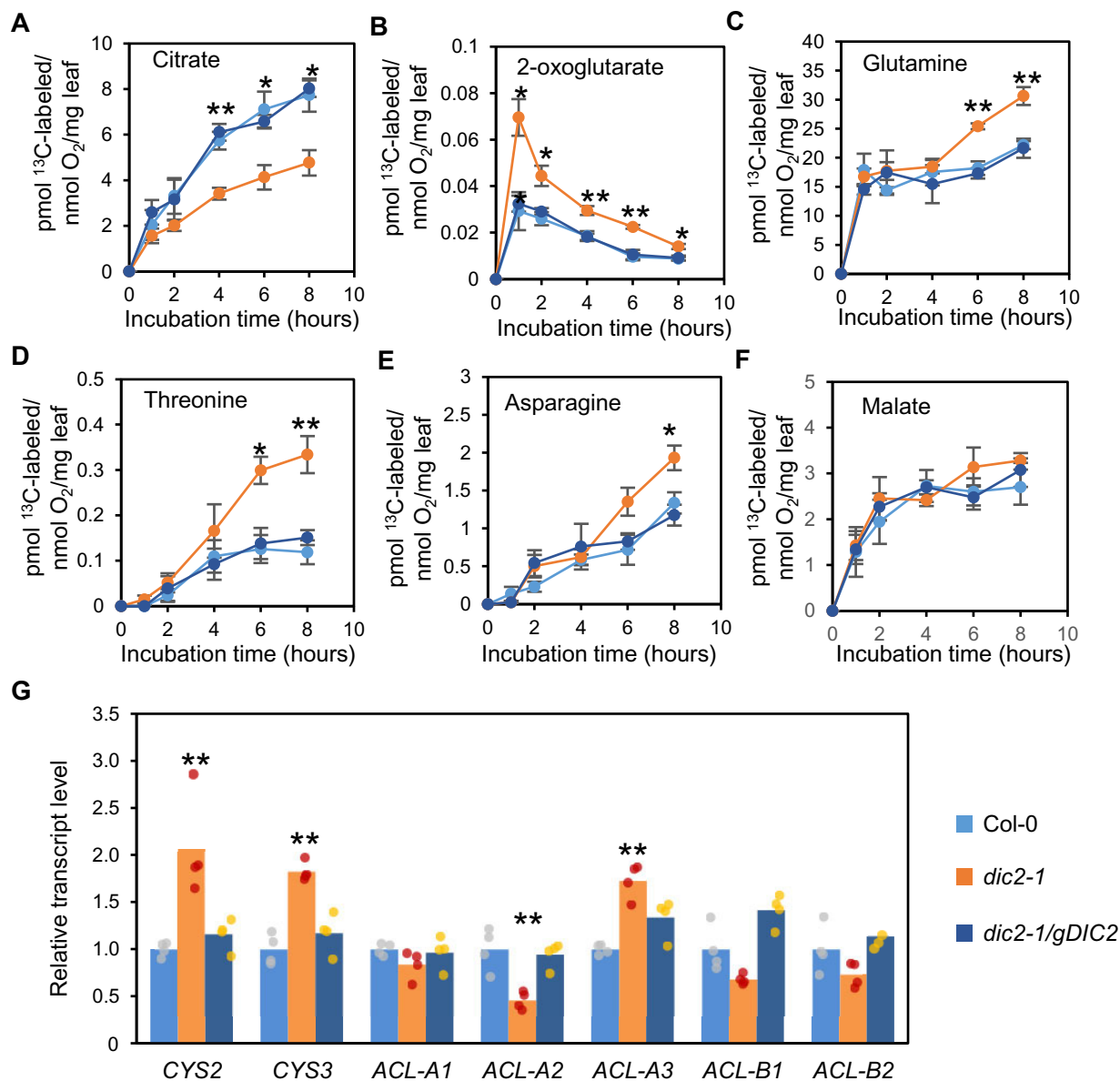
Figure 7 The loss of DIC2 causes an altered metabolite turnover of the TCA cycle in the dark. A–F, Time-courses of ^{13}C-labeling into metabolism in darkened leaf discs. Absolute abundance of total labeled metabolites as indicated is shown. Each value is expressed as the amount of indicated metabolite labeled per fresh weight of leaf per O_2 molecule consumed at the specified incubation time ($n = 4$). All ^{13}C labeling data are available in Supplemental Data Set S1. G, Gene expression analysis of peroxisomal citrate synthase and cytosolic ATP-dependent citrate lyase in leaves at night. qPCR determination of relative transcript abundances of CYS2, CYS3, ACLA-1, ACLA-2, ACLA-3, ACLB-1, and ACLB-2 in the indicated genotypes collected 15 h after dark shift. All expression values were normalized against Col-0 sample ($n = 4$), and individual data points were overlaid in dots. Values shown are mean and error bars are ± se (where appropriate), with asterisks indicating significant differences (*$P < 0.05$ or **$P < 0.01$) between dic2-1 versus Col-0 and dic2-1 versus dic2-1/gDIC2 pairs as determined by one-way ANOVA with Tukey post hoc test.

production and/or consumption by non-TCA cycle pathways could be altered to compensate for the reduction in mitochondrial citrate supply when DIC2 is absent, we measured the transcript levels of peroxisomal citrate synthase (CYS2 and CYS3; Pracharoenwattana et al., 2005) and cytosolic ATP-dependent citrate lyase (ACLA-1, ACLA-2, ACLA-3, ACLB-1, and ACLB-2; Fatland et al., 2002) in leaves collected at 15 h into the dark photoperiod (Figure 7G). We found that the expression of both CYS2 and CYS3 was significantly higher in dic2-1 than Col-0 and dic2-1/gDIC2 by two-fold. In

contrast, the expression of ACL genes in the mutant did not show consistent change, with only ACLA-2 and ACLA-3 exhibiting significant decrease and increase in transcript abundance, respectively, in the mutant when compared to other genotypes. If we assume that the expression of genes in citrate metabolism is controlled by citrate in a similar manner to other metabolic pathways observed previously (Gibon et al., 2006), it is estimated that the loss of DIC2 triggered a change in citrate contribution from 61% mitochondria to 64% peroxisomes (Supplemental Figure S9M).

In summary, these data helped to explain how a defect in mitochondrial malate/citrate exchange in *dic2-1* is significantly overcome in a whole plant metabolic context to establish day and night homeostasis and retain a viable plant albeit with stunted growth rate. Only at day to night transitions and prolonged darkness do the consequences of these unusual metabolic fluxes yield temporary gross imbalances in metabolite pools.

Discussion

Malate import and citrate export are two of the most critical fluxes that mitochondria contribute to the rest of the cellular metabolic network in plants (Fernie et al., 2004; Sweetlove et al., 2010; Lee et al., 2016). Malate plays a pivotal role in mediating metabolic redox exchange between cellular compartments (Scheibe, 2004; Selinski and Scheibe, 2019; Zhao et al., 2020), while citrate produced in mitochondria is the major source of cellular citrate when the TCA cycle operates at night in mature green leaves. To date, several mitochondrial malate carriers, including DIC2, were found to have a broad substrate preference for dicarboxylates, and limited ability to transport tricarboxylates and/or amino acids with close resemblance to dicarboxylates in vitro (Picault et al., 2002; Palmieri et al., 2008; Monné et al., 2018).

However, neither their actual contributions to mitochondrial metabolite transport nor the knockon consequences of their loss on mitochondrial metabolism in organello or in planta have been verified. Determining if these carriers are generalists or specialists in vivo and how they influence metabolism is critical in any future attempt to modify mitochondrial substrate use, or to understand if transport is a point of control in metabolic models of plant cell function. Here, we redefined DIC2, not as a generalist but as a specialist high-affinity mitochondrial malate/citrate carrier influencing both these functions in mitochondrial anaplerotic metabolism based on multiple lines of in vivo and in vitro evidence (Figure 8). While our data reveal that other carriers can facilitate these two functions, they are insufficient to maintain metabolism unperturbed. Transport of sulfate, phosphate, and other dicarboxylates by DIC2 may occur at low affinity under in vitro or specific conditions that enable these metabolites to accumulate at several magnitudes above malate and citrate levels; however, such activity is unlikely to occur in vivo given that malate and citrate are primary substrates for redox valves to connect subcellular compartments and the preferred chemical species for organic acid storage (Igamberdiev and Eprintsev, 2016).

Given the prior evidence of broad DIC1 and DIC3 substrate preference in vitro and high amino acid identity
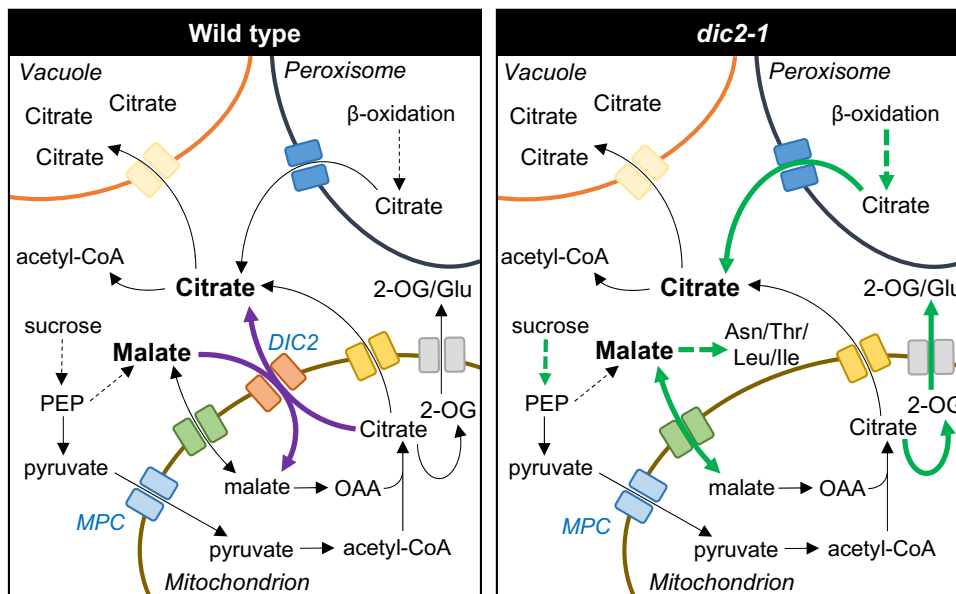

Figure 8 Schematic model of mitochondrial malate–citrate exchange for the maintenance of citrate metabolism at night. In wild-type leaves (left), DIC2 facilitates the export of citrate in exchange for malate (thick purple line) and operates in conjunction with other organic acid transporters (including other malate and citrate carriers) to support mitochondrial anaplerotic metabolism in the dark. Citrate exported from mitochondria is mostly transferred to the vacuole, with the remainder being converted to acetyl-CoA in the cytosol for the synthesis of secondary metabolism products, such as isoprenoids and flavonoids. The DIC2 loss-of-function mutant (*dic2-1*, right) significantly reduces citrate export from mitochondria but has little impact on cellular organic acid pools, including citrate. This is due to the activation of a number of compensatory mechanisms to minimize major metabolic disruptions, including (in green solid lines for single-step reactions or dashed lines for multistep pathways): increased citrate supply from β-oxidation of fatty acids in peroxisomes, faster sucrose depletion rate to increase the overall carbon supply, a higher rate of malate transport by non-DIC2 carriers and diversions of excess mitochondrial citrate and cytosolic malate into amino acid biosynthesis. However, these metabolic rearrangements fail to alleviate or cause the stunted phenotype of *dic2-1* plants, indicating that DIC2 activity is important for maintaining an overall metabolic homeostasis, particularly at night and during starvation.

among the DIC homologs, our finding that they could not complement the *dic2-1* phenotype (Figure 2B) was unexpected. However, it is not unprecedented; for example, PAPST1 and PAPST2, which are 78% identical in amino acid sequence, are responsible for 3′-phosphoadenosine 5′-phosphosulfate (PAPS)/3′-phosphoadenosine 5′-phosphate (PAP) transport and PAP/AT(D)P exchange, respectively, based on both in vitro and in vivo evidence (Gigolashvili et al., 2012; Ashykhmina et al., 2019). In a similar way, while a previous proteoliposome-based kinetic study showed that Arabidopsis DIC1 and DIC2, the closest homologs of yeast DIC, transport a variety of different dicarboxylates (Palmieri et al., 2008), such an approach alone could not accurately predict apparent substrate affinity and specificity (Figure 4), directionality of transport in intact mitochondria (Figure 3) or the in vivo consequences of DIC2 loss on transport or metabolism of other organic acids (Figures 5–7). Further experiments are required to assess how exactly DIC1 and DIC3 differ from DIC2 in terms of substrate preferences and transport kinetics.

Given the importance of mitochondria-supplied citrate to metabolism in green tissues (Gauthier et al., 2010; Cheung et al., 2014; Igamberdiev, 2020), it is expected that a complete block in mitochondrial citrate synthesis and export would result in severe reduction in post-germination vegetative growth. Indeed, a simultaneous loss of NAD-ME, mitochondrial pyruvate carrier and alanine aminotransferase activities severely disrupts seedling development, most likely due to limited supply of pyruvate for mitochondrial citrate synthesis (Le et al., 2021a). Mutants lacking the activity in one of the subunits of mitochondrial pyruvate dehydrogenase complex (mPDC) or both mMDH isoforms, which catalyze acetyl-CoA and OAA formation, respectively, required for citrate synthesis, are significantly slower in vegetative growth (Tomaz et al., 2010; Yu et al., 2012; Ohbayashi et al., 2019). Here, we also observed a reduction in vegetative growth in *dic2-1*, with decreases in citrate export by isolated mitochondria (Figure 3, H and K) and in vivo ^{13}C-glucose labeling into citrate (Figure 7A) when compared to the wild-type. Unlike mMDH and mPDC mutants, however, the steady-state pool of organic acids, including citrate, was surprisingly stable in *dic2-1* (Figure 5A). It is very likely that the increase in citrate retention in the *dic2-1* matrix triggered an increase in nighttime sucrose depletion (Figure 6B) to maintain the organic acid pools, resulting in higher R_N and malate-dependent CO_2 evolution (Figures 5, E and 6, C). Another possible pathway to compensate for a reduction in mitochondrial citrate supply is by altering fatty acid turnover via the last step of peroxisomal β-oxidation (Figure 8), given that *dic2-1* phenotypes are observed mostly during darkness and the transcripts of two peroxisomal citrate synthases (CYS2 and CYS3) are upregulated in the mutant (Figure 7G) and are more abundant in wild-type plants at night (Gibon et al., 2004; Smith et al., 2004) and during prolonged darkness (van der Graaff et al., 2006). However, possible side effects of such a strategy include a loss of synchronization in fatty acid turnover with peroxisomal citrate synthesis and export, higher triacylglycerol utilization, and lipid peroxidation

(Fan et al., 2017), which reasonably explain the increased susceptibility of *dic2-1* to dark-induced senescence (Figure 6, D and E). The requirement for an equilibrium between organellar citrate synthesis and fatty acid breakdown to prevent excess reactive oxygen species accumulation would also explain why a strong DIC2 transcriptional response is commonly observed during abiotic stress treatments, including touch and sound vibration (Ghosh et al., 2016; Van Aken et al., 2016), phosphate deficiency (Lin et al., 2011), light-to-dark transition (Lee et al., 2005), and cold, drought, and UV stresses (Kilian et al., 2007). Overall, our data strongly indicate that DIC2 transport function is integrated into whole plant metabolism as an important supplier of citrate for nighttime vacuole storage, and its absence severely limits metabolic flexibility for maintaining energy supply and redox balance in response to a sudden dark shift or a prolonged sugar starvation.

The existence of multiple modes of TCA cycle substrate transport has been proposed (Wiskich, 1977; LaNoue and Schoolwerth, 1979) but the lack of clarity as to the identity of components responsible has hindered our understanding on how they cooperate to support the integration of mitochondrial carbon metabolism into the wider cellular metabolic network (Lee and Millar, 2016). In the case of *dic2-1*, a residual rate of mitochondrial malate import and citrate export is maintained, suggesting that other carriers exist to partially compensate for the absence of DIC2 activity. It is also remarkable that in vivo cytosolic NADH/NAD$^+$ ratios in *dic2-1* leaves did not differ from wild-type throughout the night with only a glimpse of change during a light-to-dark transition (Figure 5, C and D). The homeostasis of cytosolic NAD redox state in *dic2-1* could be maintained, among other possible strategies, by (1) diverting of excess organic acids to energy-consuming biosynthesis of specific amino acids (Figures 7, G and 8) and/or (2) remobilizing excess NADH into the intermembrane space of mitochondria where it can be oxidized by external NADH dehydrogenases, thereby raising leaf respiration in the dark (Figure 5E). Studies of mitochondrial carrier mutants reported to date have been unable to directly link growth and/or metabolic phenotype with gene function (Toka et al., 2010; de Souza Chaves et al., 2019; Feitosa-Araujo et al., 2020). It is possible that, apart from functional redundancy, changes in metabolic fluxes occur without altering the overall metabolite pool or physiology, which can only be captured by sensitive measurements under specific external conditions.

In conclusion, we have refined the current understanding of how DIC2 influences mitochondrial organic acid transport and metabolism in Arabidopsis, and pinpoint how its absence leads to growth retardation. The importance of mitochondrial organic acid exchange carriers in plants has been discussed for decades, but it is only in the last decade that their identities are beginning to be unraveled through heterologous systems. By utilizing a systems approach based on reverse genetics, we demonstrate that a thorough carrier analysis in heterologous systems is only the start to reveal the in vivo role of a carrier such as DIC2. Given the lack of

genetic clarity of many plant mitochondrial carriers, it is reasonable to suspect that the true substrate specificities and in vivo metabolic influence of many other carriers have yet to be unraveled. A complete understanding of the identities of mitochondrial metabolite carriers and their substrate preferences with kinetic characteristics and transport orientation in vivo will assist in improving metabolic models, as well as refining their individual role in underpinning the remarkable flexibility of plant cell metabolism.

Materials and methods

Plant material and growth conditions

The *DIC2* T-DNA insertion lines were obtained from GABI-Kat (*dic2-1* GK-217B05, *dic2-2* GK-833F11, and *dic2-3* GK-047F03; Kleinboelting et al., 2012). These T-DNA insertion lines were screened for homozygous insertion by PCR of genomic DNA using the primer pairs according to Supplemental Table S3. Inverse PCR was carried out according to Teschner et al. (2010). The construct for genomic complementation with transgene gDIC2 was generated by amplifying the *DIC2* genomic region (including ∼2-kb upstream of start codon and ∼1-kb downstream of stop codon) from wild-type Col-0 DNA, and the resulting ∼4-kb fragment was cloned into pCAMBIA1380. Overexpression constructs were generated by amplifying the coding sequence of DIC2, DIC1, or DIC3 and inserting each of these fragments into pB7WG2 by Gateway cloning. The DIC2-GFP construct was generated by inserting DIC2 coding sequence without the stop codon into pUBC-DEST (Grefen et al., 2010) by Gateway cloning. All cloning primers were listed in Supplemental Table S3. Agrobacterium-mediated transformation of each construct was carried out by floral dipping (Zhang et al., 2006).

Arabidopsis seedlings and plants were grown under a light intensity of 100 µmol m^{-2} s^{-1} (tubular fluorescent lighting) after seeds were stratified at 4°C in the dark for 2–3 days. Plants were grown on compost supplemented with Perlite and Vermiculite (3:1:1) under continuous, short, or long photoperiod as indicated. To analyze seedling phenotypes, seeds were surface-sterilized, stratified and grown vertically for 10 days on agar plates containing half-strength MS medium, 2-mM 2-(N-morpholino)ethanesulfonic acid (MES) at pH 5.7 and 1% (w/v) agar under short-day conditions. For the isolation of mitochondria, surface-sterilized seeds were grown in Murashige and Skoog (MS) medium (1/2-strength MS medium, 2-mM MES, pH 5.7) supplemented with 1% (w/v) sucrose and 0.1% (w/v) agar for 14–16 days with gentle agitation (40–60 rpm) under long-day conditions.

Subcellular localization analysis by confocal laser scanning microscopy

A Nikon A1Si confocal microscope equipped with the following excitation and emission wavelength settings was used: 488-nm excitation and 525-nm emission for GFP, 560-nm excitation and 595-nm emission for TMRM, and 640-nm excitation and 700-nm emission for chlorophyll autofluorescence. DIC2 localization images were acquired by a NIS element AR software package (version 4.13.01, Build 916) using a 20× lens (Nikon CFI Plan Apo VC 20x 0.75 N.A.) and a 60× lens (Nikon CFI Plan Apo VC 60x 1.20 N.A. WI) and were processed using ImageJ software package.

Transcript analysis by quantitative real-time polymerase chain reaction

RNA isolation was performed using the Spectrum Plant Total RNA Kit (Sigma-Aldrich) in conjunction with on-column DNAase treatment to remove genomic DNA. cDNA was synthesized using the iScript cDNA Synthesis Kit (Bio-rad). Quantitative polymerase chain reaction was performed in a LightCycler 480 II Real Time PCR System (Roche) using the QuantiNova SYBR Green RT-PCR Kit (Qiagen) according to the manufacturer's instructions with reference genes *elongation factor-1α* (At5g60390) and *SAND family protein* (At2g28390; Czechowski et al., 2005). Relative transcript abundance was obtained by normalizing to two reference genes and the normalized values were then combined by geometric mean. All primers are listed in Supplemental Table S3.

Isolation of mitochondria, O_2 electrode measurements, enzyme activity assays, blue native electrophoresis, and metabolite uptake assays by silicone oil centrifugation

Mitochondria were isolated from 2-week-old Arabidopsis seedlings as described previously (Sweetlove et al., 2007). Single substrate-dependent O_2 consumption by purified mitochondria was measured at pH 6.8 in a computer-controlled Clark-type O_2 electrode unit according to Lee et al. (2010). In vitro activities of TCA cycle enzymes in isolated mitochondria were measured as described by Huang et al. (2015).

Digitonin-solubilized mitochondrial proteins were separated on a blue-native polyacrylamide gel electrophoresis (PAGE) according to Eubel et al. (2003), using a 4.5%–16% gradient. In-gel Complex I activity staining was carried out as outlined by Sabar et al. (2005).

Time-course measurements of substrate uptake by isolated mitochondria were carried out according to Lee et al. (2014) with modifications specified in Le et al. (2021b). Briefly, for uptake in the absence of cofactors, freshly prepared mitochondria (100 µg) were resuspended in 200-µL minimal transport buffer (250-mM sucrose, 10-mM TES, 0.5-mM ATP, pH 7.2). Uptake assays were initiated by adding radiolabeled U-[^{14}C]-malate (200 µM, Perkin Elmer) at 25°C. After the specified incubation time, the reaction was stopped immediately by rapid centrifugation (at 13,000g for 3 min at room temperature) through a 90-µL silicone oil layer (AR200, Sigma Aldrich) into the bottom sedimentation layer containing 20 µL of 10% (v/v) perchloric acid. Fractions above (supernatant) and below (containing the mitochondria pellet) the silicone oil interface were transferred to separate scintillation vials and mixed with 3 mL of Ultima Gold scintillation fluid (PerkinElmer). Radioactivity

was detected by a Beckman LS 6500 Scintillation Counter. For energized uptake, isolated mitochondria (100 µg) were resuspended in 190-µL respiratory transport medium (225-mM sucrose, 5-mM KH_2PO_4, 10-mM TES, 10-mM NaCl, 4-mM $MgSO_4$, 0.1% (w/v) BSA, 2-mM NAD, 12-µM CoA, 0.2-mM thiamine pyrophosphate, and 0.5-mM ADP, pH 6.8) and uptake was initiated by adding 50-µM or 500-µM substrate as stated. Reactions were stopped as described above, except the bottom layer contained 20 µL of 0.5-M sucrose, pH 1.5. Fractions above (extra-mitochondrial space) and bottom (pellet, mitochondria) were collected, and metabolites were methanol-extracted and detected by selective reaction monitoring mass spectrometry (liquid chromatography–selective reaction monitoring–mass spectrometry [LC–SRM–MS], see below).

Proteoliposome transport assay

The coding sequence of DIC2 without the stop codon was introduced into the yeast expression vector pYES-DEST52 (ThermoFisher Scientific) by Gateway Cloning. pYES-DIC2 or pYES-DEST52 (empty vector control) was transformed into the uracil-auxotrophic *Saccharomyces cerevisiae* strain INVSc1 (ThermoFisher Scientific) by lithium acetate transformation. To prepare microsomes, 500 mL of transformed yeast culture was inoculated overnight at 30°C according to Rautengarten et al. (2016) with slight modifications. Briefly, yeast pellet was washed several times in H_2O and was resuspended in 10-mL resuspension buffer (50-mM potassium phosphate, pH 7.1, 1.4-M sorbitol, 10-mM NaN_3, and 40-mM 2-mercaptoethanol) supplemented with 2,000 units of Lyticase (Sigma-Aldrich), followed by a 37°C incubation for 1 h with gentle shaking. The resulting spheroplasts were collected by centrifugation at 2,500g for 5 min at room temperature, washed once with wash buffer (0.8-M sorbitol, 10-mM triethanolamine/acetic acid (pH 7.2), 1-mM EDTA, 1-mM PMSF, and protease inhibitor tablet [Roche]) and lysed in 5-mL wash buffer using a Dounce homogenizer. The lysate was centrifuged at 1,500g for 5 min at 4°C to remove pellet containing large debris and the supernatant was centrifuged again at 3,000g for 5 min at 4°C. The resulting supernatant was centrifuged at 100,000g for 75 min to collect the crude microsomal fraction. This fraction was resuspended in reconstitution buffer (10-mM Tricine-KOH [pH 6.0], 50-mM potassium gluconate, and 20% glycerol).

For liposome preparation, 600 mg of soybean L-α-phosphatidylcholine (Sigma) was dissolved in 10-mL chloroform and evaporated under a stream of nitrogen for at least 45 min. The resultant film was resuspended for 2 h at 42°C in reconstitution buffer (10-mM Tricine-KOH, pH 6.0, 50-mM potassium gluconate, and 20% glycerol). Prior to reconstitution, solubilized L-α-phosphatidylcholine was extruded at 42°C using an Avanti Mini-Extruder (Avanti Polar Lipids) fitted with a 100-nm polycarbonate membrane. Approximately 400 µg microsomal proteins were reconstituted into extruded lipid at 1:13 (lipid: protein) in the presence of 10-mM internal loading substrate, 50-mM octyl-β-glucoside, and Bio-beads (BioRad Laboratories) with gentle

agitation for 2 h at room temperature. Unincorporated components were removed from substrate-loaded proteoliposomes by passing through Sephadex G50 (medium, GE Healthcare) several times.

Aliquots of 200-µL proteoliposomes were incubated with specified substrates (pH adjusted to 6.0) at 25°C for indicated times. Substrates that remained on the outside of proteoliposomes were rapidly removed by passing the reaction through a pre-packed 2-mL Sephadex G50 column. Proteins and metabolites in the resulting supernatant were extracted by chloroform/methanol extraction. Following liquid removal and sample resuspension, 3-nitrophenylhydrazine-derivatised metabolites were quantified by LC–SRM–MS (see below). Extracted proteins were separated on mini-PROTEAN TGX stain-free gels and visualized directly without staining using the Gel Doc XR+ with Image Lab software (Bio-Rad Laboratories). Proteins were then transferred onto a PVDF membrane for immunodetection with the monoclonal anti-V5 antibodies (1:10,000 dilution; ThermoFisher Scientific, Catalogue number R96025) using the Amersham Imager 680 (GE Healthcare).

Leaf gas exchange, chlorophyll fluorescence, and respiration measurements

Measurements of gas-exchange parameters were carried out using a LI-6400 XT infrared gas analyser (Li-Cor). After at least 2 h of illumination, measurements were carried out using fully developed leaves from at least 8-week-old short-day grown plants. Prior to each measurement, leaf was acclimated in the enclosed 60-mm^2 chamber to 22°C, relative humidity 70%, and a CO_2 concentration of 400 ppm with light intensity of 250 µmol m^{-2} s^{-1}. A series of light intensities (0, 50, 100, 250, 500, 700 µmol m^{-2} s^{-1}) was applied and the following parameters were then recorded: CO_2 assimilation rate, stomatal conductance, and transpiration rate. For the analysis of post-illumination bursts, leaf was equilibrated in a chamber to 22°C and relative humidity 70%, with light intensity of 1,000 µmol m^{-2} s^{-1} and CO_2 concentration of 100 ppm. CO_2 assimilation rate in the light was monitored for 3 min before dark shift (i.e. photosynthetic active radiation [PAR] = 0 µmol m^{-2} s^{-1}) and CO_2 evolution rate was monitored for 2.5 min.

Chlorophyll fluorescence measurements were carried out using the IMAGING-PAM Maxi Version Chlorophyll Fluorometer (WALZ). Plants were acclimated in the dark for at least 15 min before F_v/F_m, PSII quantum yield during illumination (Y[II]), photosynthetic electron transport rate, and nonphotochemical quenching were monitored at increasing actinic light intensities and plotted as light response curves.

Dark respiration was measured in dark-adapted, fully expanded leaves using a Q2 O_2 sensor (Astec-Global) as previously described (O'Leary et al., 2017). O_2 concentration in a sealed 850-µL capacity tube with a single leaf disc (6.5-mm diameter, with a total of 40–60 mg fresh weight) floated on leaf respiration buffer (10-mM HEPES, 10-mM MES, and 0.2-mM $CaCl_2 2H_2O$, pH 7.2) was measured. For leaf $^{14}CO_2$

evolution measurements, leaf discs were floated on leaf respiration buffer containing $\sim$0.5 KBq mL^{-1} of U-^{14}C-malate or U-^{14}C-leucine (Perkin Elmer). Evolved ^{14}CO$_2$ trapped in KOH-soaked filter paper and total radiolabel extracted from leaf discs were measured by a liquid scintillation counter (Beckman Coulter).

Analysis of NAD redox dynamics

All experiments were carried out with leaf discs of 6-week-old A. thaliana plants grown under long-day conditions (16-h light/8-h dark). Microscopy procedures described in Wagner et al. (2015) were used as guideline for ratiometric sensor monitoring with the modification that samples were mounted between two cover slips (22 × 40 mm, VWR). Dynamic changes under dark-light conditions were monitored as described by Elsässer et al. (2020) with a confocal laser scanning microscope (Zeiss LSM 780, attached to an Axio Observer.Z1; Carl Zeiss Microscopy) using the 10× objective (Plan-Apochromat, 0.3 M27). Excitation was set at 405 nm (T-Sapphire) and 543 nm (mCherry), emission was collected at 499–544 nm (T-Sapphire) and 588–624 nm (mCherry). The ZEN Experiment Designer software module (Carl Zeiss) was used to program time series with varying scanning cycles and illumination times. A custom-made device with an implemented cold white LED stripe (Pferdekaemper, Menden, Germany) was used to apply actinic light with an intensity of 220 µmol m^{-2} s^{-1}. Time series with Peredox-mCherry were performed with the following regime: (1) 15 min in the dark of 30 scans with 30-s interval; (2) 15 min of illumination with 8 loops of 15-s light followed by 3.2-s scan and 26 loops of 30 s light followed by 3.2-s scan; (3) 15 min in the dark of 30 scans with 30-s interval.

For in vivo measurements of NAD redox changes, leaf discs stably expressing cytosolic Peredox-mCherry were subjected to multiwell plate reader-based fluorimetry, as described in De Col et al. (2017). Plant material was submerged in 200-µL assay medium (10-mM HEPES, 10-mM MES, and 0.2-mM CaCl$_2$, pH 7.2) in a transparent 96-well plate (NUNC). Peredox-mCherry fluorescence was recorded in a CLARIOstar microplate reader (BMG Labtech, Ortenberg, Germany). The chromophores T-Sapphire and mCherry were excited at 400 ± 10 nm and 570 ± 10 nm, and emission collected at 515 ± 7.5 nm and 610 ± 5 nm, respectively. Samples were analyzed employing top optics with focal height of 8.0 mm, incubation temperature at 25°C, well-multichromatic monitoring, 50 flashes per cycle and double orbital shaking at 400 rpm for 10 s before each measurement cycle. Background fluorescence of control plants without sensor expression was recorded in parallel and subtracted from all data before analysis. Mounting of the leaf discs was performed, except for the use of a green LED head torch, in the dark at the end of the night shortly prior to the night-to-day transition. After recording the baseline, plates were exposed to actinic light under white LEDs with a photon flux density of 120 µmol m^{-2} s^{-1} for in total 8 h, except for 3-min-long interruptions allowing for fluorometric sensor recording at indicated time points. For the

subsequent dark phase, the plate was kept inside the plate reader (dark) and measurements were performed every 30 min.

Metabolite extraction from plant tissues

Plant tissues ($\sim$25 mg for general metabolite analysis or $\sim$50 mg for isotope labeling experiments) were collected at specified time points and immediately snap-frozen in liquid nitrogen. Samples were ground to fine powder and 500 µL of cold metabolite extraction solution (90% [v/v] methanol, spiked with 2-mg·mL^{-1} ribitol, 6-mg·mL^{-1} adipic acid, and 2 mg·mL^{-1} and ^{13}C-leucine as internal standards). Samples were immediately vortexed and shaken at 1,400 rpm for 20 min at 75°C. Cell debris was removed by centrifugation at 20,000g for 5 min at room temperature. For each sample, 100 µL (400 µL for isotope labeling experiments) of supernatant was transferred to a new tube and either proceeded to derivatization for LC–MS analysis or dried using a SpeedVac.

Analyses of sugars by gas chromatography–mass spectrometry

For gas chromatography–mass spectrometry analysis of sugars, dried samples were dissolved in 20 µL of pyridine in methoxylamine hydrochloride (20 mg mL^{-1}) and incubated at 30°C for 90 min at 1,200 rpm. Then, 30 µL of N-methyl-N-(trimethylsilyl)-trifluoroacetamide was added to each sample and allowed to react for 30 min at 37°C at 1,400 rpm. The derivatized metabolite samples were analyzed by an Agilent 6890 gas chromatograph coupled with a 7683B Automatic Liquid Sampler and a 5973N mass selective detector, and fitted with an Agilent VF-5ms capillary column (30 m × 0.25 µm, 0.25 mm internal diameter) and a 10 m integrated guard column. The helium carrier gas flow rate was 1 mL·min^{-1}. For the 58.5-min temperature gradient, the GC oven was held at the initial temperature of 70°C for 1 min, increased to 76°C at the rate of 1°C·min^{-1} and then to 325°C at the rate of 6°C·min^{-1} where it was held at 325°C for 10 min. The inlet temperature, MS source temperature and quadrupole temperature were 300°C, 230°C, and 150°C, respectively. The MS detector m/z scan range was 40–600. Data were analyzed using MassHunter Quantitative Analysis Software (version B.07.01, Build 7.1.524.0). Metabolites were quantified by comparing the integrated peak area with a calibration curve obtained using authentic standards, and normalized against fresh weight and ribitol internal standard.

Analyses of organic acids and amino acids by multiple reaction monitoring using LC–SRM–MS

For LC–MS analysis of organic acids, sample derivatization was carried out based on a previously published method with modifications (Han et al., 2013). Briefly, for each 100 µL of sample, 50 µL of 250-mM 3-nitrophenylhydrazine in 50% methanol, 50 µL of 150-mM 1-ethyl-3-(3-dimethylamino-propyl) carbodiimide in methanol, and 50 µL of 7.5% pyridine in 75% methanol were mixed and allowed to react on ice for 60 min. To terminate the reaction, 50 µL of 2-mg mL^{-1} butylated-hydroxytoluene in methanol was added,

followed by the addition of 700 μL of water. Derivatized organic acids were separated on a Phenomenex Kinetex XB-C18 column (50 × 2.1 mm, 5 μm particle size) using 0.1% (v/v) formic acid in water (solvent A) and methanol with 0.1% formic acid (solvent B) as the mobile phase. The elution gradient was 18% B at 1 min, 90% B at 10 min, 100% B at 11 min, 100% B at 12 min, 18% B at 13 min, and 18% B at 20 min. The column flow rate was 0.3 mL·min^{-1}, and the column temperature was maintained at 40°C. The Agilent 6430 Triple Quadrupole mass spectrometer (QQQ-MS) was operated in negative ion mode in the SRM mode.

For measuring amino acids, dried samples were resuspended in 500-μL HPLC-grade water before they were filtered to remove insoluble debris. Metabolites were separated on an Agilent Poroshell 120 Bonus-BP column (100 × 2.1 mm, 2.7-μm internal diameter) using 0.1% formic acid in water (solvent A) and acetonitrile with 0.1% formic acid (solvent B) as the mobile phase. For the analysis of amino acids and sugars, the elution gradient was 0% B at 1 min, 1% B at 4 min, 10% B at 6 min, 100% B at 6.5 min, 100% B at 8 min, 0% B at 8.5 min, and 0% B at 15 min. The column flow rate was 0.25 mL·min^{-1}, and the column temperature was kept at 40°C. The QQQ-MS was operated in positive ion mode in SRM mode.

A 0.5 μL or a 15 μL aliquot of each sample was injected and analyzed by an Agilent 1100 HPLC system coupled to a QQQ-MS equipped with an electrospray ion source. Data acquisition and LC-MS control were done using the Agilent MassHunter Data Acquisition software (version B06.00 Build 6.0.6025.4). The autosampler was kept at 10°C. The QQQ-MS was operated in SRM mode using the following operation settings: capillary voltage, 4,000 V; drying N2 gas and temperature, 11 L·min^{-1} and 125°C, respectively; Nebulizer, 15 psi. All optimized SRM transitions for each target are listed in Supplemental Table S4. Data analysis was carried out using MassHunter Quantitative Analysis Software (version B.07.01, Build 7.1.524.0). Metabolites were quantified by comparing the integrated peak area with a calibration curve obtained using authentic standards and normalized against fresh weight and internal standards.

Dynamic ^{13}C-glucose labeling of Arabidopsis leaf discs and analysis of labeled metabolites by time-of-flight mass spectrometry

Leaf discs (∼50 mg) were prepared from short-day grown (8-h light/16-h dark) plants 1 h before the end of a normal light photoperiod. They were floated on leaf respiratory buffer containing 20-mM U-^{13}C-glucose (99% purity, Sigma Aldrich). At the specified incubation time, leaf discs were briefly washed with respiratory buffer to remove excess labeled glucose and frozen in liquid nitrogen for metabolite extraction as stated above.

Analyses of unlabeled and labeled metabolites were performed using an Agilent 1100 HPLC system coupled to an Agilent 6510 Quadrupole/Time-of-Flight (Q-TOF) mass spectrometer equipped with an electrospray ion source. Data

acquisition and LC–MS control were carried out using the Agilent MassHunter Data Acquisition software (version B.02.00). Separation of metabolites was performed using a Luna C18 column (Phenomenex; 150 × 2 mm, 3-μm particle size). The mobile phase consisted of 97:3 water: methanol with 10-mM tributylamine and 15-mM acetic acid (solvent A) and 100% methanol (solvent B). The gradient program was 0% B 0 min, 1% B 5 min, 5% B 15 min, 10% B 22 min, 25% B 24 min, 27% B 35 min, 29% B 80 min, 95% B 81 min, 95% B 82 min, 0% B 83 min, and 0% B 97 min. The flow rate was 0.2 mL·min^{-1}, with column temperature kept at 35°C, autosampler was cooled to 10°C and injection volume was 30 μL. The Q-TOF was operated in MS mode with negative ion polarity using the following operation settings: capillary voltage, 4,000 V; drying N$_2$ gas and temperature, 10 L·min^{-1} and 250°C respectively; Nebulizer, 30 psi. Fragmentor, skimmer, and octopole radio frequency (Oct1 RF Vpp) voltages were set to 110 V, 65 V, and 750 V, respectively. The scan range was 70–1,200 m/z and spectra were collected at 4.4 spectra/s, which corresponded to 2,148 transients/spectrum. MS scan peaks of all the possible mass isotopologs were integrated using MassHunter Quantitative Analysis Software (version B.07.01, Build 7.1.524.0). Extracted peak matrices were processed using IsoCor (Millard et al., 2019) to correct for the contribution of naturally occurring isotopes. Relative isotopomer abundance for each metabolite and percentages of ^{13}C enrichment were calculated according to Araújo et al. (2014). Metabolite quantitation was carried out based on calibration curves obtained with unlabeled authentic standards.

Relative quantitation of mitochondrial protein abundances by LC–MRM–MS

Multiple reaction monitoring (MRM) was carried out exactly as described previously (James et al., 2019), except trypsin was added to the protein samples in a mass ratio of 1:20. Peptide abundances from each sample were normalized against Voltage-dependent anion channel (VDAC) in which its abundance was identical between mitochondria from Col-0, dic2-1, and dic2-1/gDIC2 based on immunoblotting. Transitions used for multiple reaction monitoring of VDAC, DIC2, TCA cycle enzymes, pyruvate dehydrogenase, and NAD-ME are provided in Supplemental Data Set S2.

Statistical analysis

All statistical analyses were performed either with Excel (Student's t test) or RStudio (analysis of variance (ANOVA) with Tukey Posthoc analysis, Shapiro–Wilk normality test, and Levene's test). Kinetic parameters K_m and V_{max} were determined from the Michaelis–Menten equation using the Enzyme Kinetic module in SigmaPlot (version 12.5). Statistical tests and replicate number are as indicated in figure legends; all statistical evidence is provided in Supplemental Data Set S3.

Accession numbers

Sequence data from this article can be found in the Arabidopsis Genome Initiative or GenBank/EMBL databases under the following accession numbers: DIC1 (At2g22500), DIC2 (At4g25470), DIC3 (At5g09470), VDAC1 (At3g01280), SAND (At2g28390), EF-1α (At5g60390), CSY2 (At3g58750), CSY3 (At2g42790), ACLA-1 (At1g10670), ACLA-2 (At1g60810), ACLA-3 (At1g09430), ACLB-1 (At3g06650), ACLB-2 (At5g49460), SEN1 (At4g35770), WRKY53 (At2g28390), and SAG101 (At5g14930). All data generated or analyzed during this study are included in this published article and its supplementary information files.

Supplemental data

The following materials are available in the online version of this article.

Supplemental Figure S1. Subcellular localization of DIC2 in Arabidopsis.

Supplemental Figure S2. Phenotypes of *dic2-1* and *dic2-1/gDIC2* plants.

Supplemental Figure S3. Characteristics of isolated mitochondria.

Supplemental Figure S4. Malate and citrate feeding of isolated mitochondria.

Supplemental Figure S5. Substrate preference of DIC2 in microsome-reconstituted liposomes.

Supplemental Figure S6. Changes in photosynthetic and respiratory parameters in *dic2-1* and *dic2-1/gDIC2* plants.

Supplemental Figure S7. The role of DIC2 in controlling amino acid pool and sugar use in the light and dark.

Supplemental Figure S8. Effects of extended dark treatment on Arabidopsis phenotypes.

Supplemental Figure S9. Incorporation of ^{13}C-glucose into metabolism of leaf discs in the dark.

Supplemental Table S1. Relative expression of DIC2, DIC1, and DIC3 in Col-0, *dic2-1*, and complemented lines as determined by qPCR.

Supplemental Table S2. Kinetic properties of TCA cycle enzymes in isolated mitochondria.

Supplemental Table S3. A list of primers used in this study.

Supplemental Table S4. A list of LC–MRM–MS transitions of metabolites.

Supplemental Data Set S1. 13C labeling into selected organic acids and amino acids.

Supplemental Data Set S2. List of LC–MRM–MS transitions of peptides.

Supplemental Data Set S3. All statistical analysis.

Acknowledgments

We thank Dr Brendan O'Leary (The University of Western Australia) for a critical reading of the manuscript.

Funding

Conflict of interest statement. The authors declare that they have no conflict of interest.

References

Araújo WL, Tohge T, Nunes-Nesi A, Obata T, Fernie AR (2014) Analysis of kinetic labeling of amino acids and organic acids by GC-MS. *In* M Dieuaide-Noubhani, AP Alonso, eds, Plant Metabolic Flux Analysis: Methods and Protocols. Humana Press, Totowa, NJ, pp 107–119

Ashykhmina N, Lorenz M, Frerigmann H, Koprivova A, Hofsetz E, Stührwohldt N, Flügge U-I, Haferkamp I, Kopriva S, Gigolashvili T (2019) PAPST2 plays critical roles in removing the stress signaling molecule 3′-phosphoadenosine 5′-phosphate from the cytosol and its subsequent degradation in plastids and mitochondria. Plant Cell **31**: 231–249

Baud S, Guyon V, Kronenberger J, Wuillème S, Miquel M, Caboche M, Lepiniec L, Rochat C (2003) Multifunctional acetyl-CoA carboxylase 1 is essential for very long chain fatty acid elongation and embryo development in Arabidopsis. Plant J **33**: 75–86

Bernard SM, Habash DZ (2009) The importance of cytosolic glutamine synthetase in nitrogen assimilation and recycling. New Phytol **182**: 608–620

Bykova NV, Møller IM, Gardeström P, Igamberdiev AU (2014) The function of glycine decarboxylase complex is optimized to maintain high photorespiratory flux via buffering of its reaction products. Mitochondrion **19**: 357–364

Carrari F, Nunes-Nesi A, Gibon Y, Lytovchenko A, Loureiro ME, Fernie AR (2003) Reduced expression of aconitase results in an enhanced rate of photosynthesis and marked shifts in carbon partitioning in illuminated leaves of wild species tomato. Plant Physiol **133**: 1322–1335

Chen WW, Freinkman E, Wang T, Birsoy K, Sabatini DM (2016) Absolute quantification of matrix metabolites reveals the dynamics of mitochondrial metabolism. Cell **166**: 1324–1337.e1311

Cheung CYM, Poolman MG, Fell DA, Ratcliffe RG, Sweetlove LJ (2014) A diel flux balance model captures interactions between light and dark metabolism during day-night cycles in C$_3$ and Crassulacean acid metabolism leaves. Plant Physiol **165**: 917–929

Czechowski T, Stitt M, Altmann T, Udvardi MK, Scheible W-R (2005) Genome-wide identification and testing of superior reference genes for transcript normalization in Arabidopsis. Plant Physiol **139**: 5–17

Day DA, Hanson JB (1977a) Effect of phosphate and uncouplers on substrate transport and oxidation by isolated corn mitochondria. Plant Physiol **59**: 139–144

Day DA, Hanson JB (1977b) Pyruvate and malate transport and oxidation in corn mitochondria. Plant Physiol **59**: 630–635

De Col V, Fuchs P, Nietzel T, Elsässer M, Voon CP, Candeo A, Seeliger I, Fricker MD, Grefen C, Møller IM, et al. (2017). ATP sensing in living plant cells reveals tissue gradients and stress dynamics of energy physiology. eLife **6**: e26770

de Oliveira Dal'Molin CG, Quek L-E, Palfreyman RW, Brumbley SM, Nielsen LK (2010) C4GEM, a genome-scale metabolic model to study C$_4$ plant metabolism. Plant Physiol **154**: 1871–1885

de Souza Chaves I, Feitosa-Araújo E, Florian A, Medeiros DB, da Fonseca-Pereira P, Charton L, Heyneke E, Apfata JAC, Pires MV, Mettler-Altmann T, et al. (2019). The mitochondrial NAD$^+$ transporter (NDT1) plays important roles in cellular NAD$^+$ homeostasis in *Arabidopsis thaliana*. Plant J **100**: 487–504

Douce R, Mannella CA, Bonner WD (1973) The external NADH dehydrogenases of intact plant mitochondria. Biochim Biophys Acta **292**: 105–116

Elsässer M, Feitosa-Araujo E, Lichtenauer S, Wagner S, Fuchs P, Giese J, Kotnik F, Hippler M, Meyer AJ, Maurino VG, et al. (2020) Photosynthetic activity triggers pH and NAD redox signatures across different plant cell compartments. bioRxiv, 2020.2010.2031.363051 (November 1, 2020)

Eubel H, Jänsch L, Braun H-P (2003) New insights into the respiratory chain of plant mitochondria. Supercomplexes and a unique composition of Complex II. Plant Physiol 133: 274–286

Fahien LA, Kmiotek EH, MacDonald MJ, Fibich B, Mandic M (1988) Regulation of malate dehydrogenase activity by glutamate, citrate, alpha-ketoglutarate, and multienzyme interaction. J Biol Chem 263: 10687–10697

Fan J, Yu L, Xu C (2017) A central role for triacylglycerol in membrane lipid breakdown, fatty acid β-oxidation, and plant survival under extended darkness. Plant Physiol 174: 1517–1530

Fatland BL, Nikolau BJ, Wurtele ES (2005) Reverse genetic characterization of cytosolic acetyl-CoA generation by ATP-citrate lyase in Arabidopsis. Plant Cell 17: 182–203

Fatland BL, Ke J, Anderson MD, Mentzen WI, Cui LW, Allred CC, Johnston JL, Nikolau BJ, Wurtele ES (2002) Molecular characterization of a heteromeric ATP-citrate lyase that generates cytosolic acetyl-Coenzyme A in Arabidopsis. Plant Physiology 130, 740–756.

Feitosa-Araujo E, Chaves IdS, Florian A, da Fonseca-Pereira P, Apfata JAC, Heyneke E, Medeiros DB, Pires MV, Mettler-Altmann T, Neuhaus HE, et al. (2020). Down-regulation of a mitochondrial NAD$^+$ transporter (NDT2) alters seed production and germination in Arabidopsis. Plant Cell Physiol 61: 897–908

Fernie AR, Carrari F, Sweetlove LJ (2004) Respiratory metabolism: glycolysis, the TCA cycle and mitochondrial electron transport. Curr Opin Plant Biol 7: 254–261

Foyer CH, Noctor G, Hodges M (2011) Respiration and nitrogen assimilation: targeting mitochondria-associated metabolism as a means to enhance nitrogen use efficiency. J Exp Bot 62: 1467–1482

Fuchs P, Rugen N, Carrie C, Elsässer M, Finkemeier I, Giese J, Hildebrandt TM, Kühn K, Maurino VG, Ruberti C, et al. (2020). Single organelle function and organization as estimated from Arabidopsis mitochondrial proteomics. Plant J 101: 420–441

Gauthier PPG, Bligny R, Gout E, Mahé A, Nogués S, Hodges M, Tcherkez GGB (2010) In folio isotopic tracing demonstrates that nitrogen assimilation into glutamate is mostly independent from current CO_2 assimilation in illuminated leaves of Brassica napus. New Phytol 185: 988–999

Gerhardt R, Heldt HW (1984) Measurement of subcellular metabolite levels in leaves by fractionation of freeze-stopped material in nonaqueous media. Plant Physiol 75: 542–547

Gerhardt R, Stitt M, Heldt HW (1987) Subcellular metabolite levels in spinach leaves. Regulation of sucrose synthesis during diurnal alterations in photosynthetic partitioning. Plant Physiol 83: 399–407

Ghosh R, Mishra RC, Choi B, Kwon YS, Bae DW, Park S-C, Jeong M-J, Bae H (2016) Exposure to sound vibrations lead to transcriptomic, proteomic and hormonal changes in Arabidopsis. Scient Rep 6: 33370

Gibon Y, Usadel B, Blaesing OE, Kamlage B, Hoehne M, Trethewey R, Stitt M (2006) Integration of metabolite with transcript and enzyme activity profiling during diurnal cycles in Arabidopsis rosettes. Genome Biol 7: R76

Gibon Y, Blaesing OE, Hannemann J, Carillo P, Höhne M, Hendriks JHM, Palacios N, Cross J, Selbig J, Stitt M (2004) A robot-based platform to measure multiple enzyme activities in Arabidopsis using a set of cycling assays: comparison of changes of enzyme activities and transcript levels during diurnal cycles and in prolonged darkness. Plant Cell 16: 3304–3325

Gigolashvili T, Geier M, Ashykhmina N, Frerigmann H, Wulfert S, Krueger S, Mugford SG, Kopriva S, Haferkamp I, Flügge U-I (2012) The Arabidopsis thylakoid ADP/ATP carrier TAAC has an additional role in supplying plastidic phosphoadenosine 5′-phosphosulfate to the cytosol. Plant Cell 24: 4187–4204

Grefen C, Donald N, Hashimoto K, Kudla J, Schumacher K, Blatt MR (2010) A ubiquitin-10 promoter-based vector set for fluorescent protein tagging facilitates temporal stability and native protein distribution in transient and stable expression studies. Plant J 64: 355–365

Han J, Gagnon S, Eckle T, Borchers CH (2013) Metabolomic analysis of key central carbon metabolism carboxylic acids as their 3-nitrophenylhydrazones by UPLC/ESI-MS. Electrophoresis 34: 2891–2900

Hatch M, Kagawa T (1974) Activity, location and role of NAD malic enzyme in leaves with C_4-pathway photosynthesis. Funct Plant Biol 1: 357–369

He Y, Gan S (2002) A gene encoding an acyl hydrolase is involved in leaf senescence in Arabidopsis. Plant Cell 14: 805–815

Hildebrandt TM, Nunes Nesi A, Araújo WL, Braun H-P (2015) Amino acid catabolism in plants. Mol Plant 8: 1563–1579

Hooks MA, Allwood JW, Harrison JKD, Kopka J, Erban A, Goodacre R, Balk J (2014) Selective induction and subcellular distribution of ACONITASE 3 reveal the importance of cytosolic citrate metabolism during lipid mobilization in Arabidopsis. Biochem J 463: 309–317

Huang S, Lee CP, Millar AH (2015) Activity assay for plant mitochondrial enzymes. In J Whelan, MW Murcha, eds, Plant Mitochondria: Methods and Protocols. Springer New York, New York, pp 139–149

Hüdig M, Maier A, Scherrers I, Seidel L, Jansen EEW, Mettler-Altmann T, Engqvist MKM, Maurino VG (2015) Plants possess a cyclic mitochondrial metabolic pathway similar to the mammalian metabolic repair mechanism involving malate dehydrogenase and L-2-hydroxyglutarate dehydrogenase. Plant Cell Physiol 56: 1820–1830

Igamberdiev AU (2020) Citrate valve integrates mitochondria into photosynthetic metabolism. Mitochondrion 52: 218–230

Igamberdiev AU, Eprintsev AT (2016) Organic acids: the pools of fixed carbon involved in redox regulation and energy balance in higher plants. Front Plant Sci 7: 1042

Igamberdiev AU, Romanowska E, Gardeström P (2001) Photorespiratory flux and mitochondrial contribution to energy and redox balance of barley leaf protoplasts in the light and during light-dark transitions. J Plant Physiol 158: 1325–1332

James AM, Haywood J, Leroux J, Ignasiak K, Elliott AG, Schmidberger JW, Fisher MF, Nonis SG, Fenske R, Bond CS, et al. (2019). The macrocyclizing protease butelase 1 remains autocatalytic and reveals the structural basis for ligase activity. Plant J 98: 988–999

Journet E-P, Neuburger M, Douce R (1981) Role of glutamate-oxaloacetate transaminase and malate dehydrogenase in the regeneration of NAD$^+$ for glycine oxidation by spinach leaf mitochondria. Plant Physiol 67: 467–469

Kearney EB, Ackrell BAC, Mayr M (1972) Tightly bound oxalacetate and the activation of succinate dehydrogenase. Biochem Biophys Res Commun 49: 1115–1121

Kilian J, Whitehead D, Horak J, Wanke D, Weinl S, Batistic O, D'Angelo C, Bornberg-Bauer E, Kudla J, Harter K (2007) The AtGenExpress global stress expression data set: protocols, evaluation and model data analysis of UV-B light, drought and cold stress responses. Plant J 50: 347–363

Kleinboelting N, Huep G, Kloetgen A, Viehoever P, Weisshaar B (2012) GABI-Kat SimpleSearch: new features of the Arabidopsis thaliana T-DNA mutant database. Nucleic Acids Res 40: D1211–D1215

Klingenberg M (1979) Overview on mitochondrial metabolite transport systems. Methods Enzymol 56: 245–252

Kromer S (1995) Respiration during photosynthesis. Annu Rev Plant Physiol Plant Mol Biol 46: 45–70

Lance C, Rustin P (1984) The central role of malate in plant metabolism. Physiol Vég **22**: 625–641

Landschütze V, Willmitzer L, Müller-Röber B (1995) Inhibition of flower formation by antisense repression of mitochondrial citrate synthase in transgenic potato plants leads to a specific disintegration of the ovary tissues of flowers. EMBO J **14**: 660–666

LaNoue KF, Schoolwerth AC (1979) Metabolite transport in mitochondria. Annu Rev Biochem **48**: 871–922

Le XH, Lee CP, Millar AH (2021a) The mitochondrial pyruvate carrier (MPC) complex is one of three pyruvate-supplying pathways that sustain Arabidopsis respiratory metabolism. Plant Cell **33**: 2776–2793

Le XH, Millar AH, Lee CP (2021b) Assessing the kinetics of metabolite uptake and utilisation by isolated mitochondria using selective reaction monitoring-mass spectrometry (SRM-MS). Methods Mol Biol **2363** DOI: 10.1007/978-1-0716-1653-6_8

Lee CP, Millar AH (2016) The plant mitochondrial transportome: balancing metabolic demands with energetic constraints. Trends Plant Sci **21**: 662–676

Lee CP, Eubel H, Millar AH (2010) Diurnal changes in mitochondrial function reveal daily optimization of light and dark respiratory metabolism in Arabidopsis. Mol Cell Proteom **9**: 2125–2139

Lee CP, Wirtz M, Hell R (2014) Evidence for several cysteine transport mechanisms in the mitochondrial membranes of *Arabidopsis thaliana*. Plant Cell Physiol **55**: 64–73

Lee CP, Maksaev G, Jensen GS, Murcha MW, Wilson ME, Fricker M, Hell R, Haswell ES, Millar AH, Sweetlove LJ (2016) MSL1 is a mechanosensitive ion channel that dissipates mitochondrial membrane potential and maintains redox homeostasis in mitochondria during abiotic stress. Plant J **88**: 809–825

Lee D, Polisensky DH, Braam J (2005) Genome-wide identification of touch- and darkness-regulated Arabidopsis genes: a focus on calmodulin-like and XTH genes. New Phytol **165**: 429–444

Lin WD, Liao YY, Yang TJ, Pan CY, Buckhout TJ, Schmidt W (2011) Coexpression-based clustering of Arabidopsis root genes predicts functional modules in early phosphate deficiency signaling. Plant Physiol **155**: 1383–1402

Macrae AR (1971a) Effect of pH on the oxidation of malate by isolated cauliflower bud mitochondria. Phytochemistry **10**: 1453–1458

Macrae AR (1971b) Isolation and properties of a 'malic' enzyme from cauliflower bud mitochondria. Biochem J **122**: 495–501

Miao Y, Zentgraf U (2007) The antagonist function of Arabidopsis WRKY53 and ESR/ESP in leaf senescence is modulated by the jasmonic and salicylic acid equilibrium. Plant Cell **19**: 819–830

Millard P, Delépine B, Guionnet M, Heuillet M, Bellvert F, Létisse F (2019) IsoCor: isotope correction for high-resolution MS labeling experiments. Bioinformatics **35**: 4484–4487

Monné M, Daddabbo L, Gagneul D, Obata T, Hielscher B, Palmieri L, Miniero DV, Fernie AR, Weber APM, Palmieri F (2018) Uncoupling proteins 1 and 2 (UCP1 and UCP2) from *Arabidopsis thaliana* are mitochondrial transporters of aspartate, glutamate, and dicarboxylates. J Biol Chem **293**: 4213–4227

O'Leary BM, Lee CP, Atkin OK, Cheng R, Brown TB, Millar AH (2017) Variation in leaf respiration rates at night correlates with carbohydrate and amino acid supply. Plant Physiol **174**: 2261–2273

Oh SA, Lee SY, Chung IK, Lee C-H, Nam HG (1996) A senescence-associated gene of *Arabidopsis thaliana* is distinctively regulated during natural and artificially induced leaf senescence. Plant Mol Biol **30**: 739–754

Ohbayashi I, Huang S, Fukaki H, Song X, Sun S, Morita MT, Tasaka M, Millar AH, Furutani M (2019) Mitochondrial pyruvate dehydrogenase contributes to auxin-regulated organ development. Plant Physiol **180**: 896–909

Oliver DJ, Nikolau BJ, Wurtele ES (2009). Acetyl-CoA—life at the metabolic nexus. Plant Sci **176**: 597–601

Palmieri L, Picault N, Arrigoni R, Besin E, Palmieri F, Hodges M (2008) Molecular identification of three *Arabidopsis thaliana* mitochondrial dicarboxylate carrier isoforms: organ distribution, bacterial expression, reconstitution into liposomes and functional characterization. Biochem J **410**: 621–629

Picault N, Palmieri L, Pisano I, Hodges M, Palmieri F (2002) Identification of a novel transporter for dicarboxylates and tricarboxylates in plant mitochondria. Bacterial expression, reconstitution, functional characterization, and tissue distribution. J Biol Chem **277**: 24204–24211

Pracharoenwattana I, Cornah JE, Smith SM (2005) Arabidopsis peroxisomal citrate synthase is required for fatty acid respiration and seed germination. Plant Cell **17**: 2037–2048

Raghavendra AS, Padmasree K (2003) Beneficial interactions of mitochondrial metabolism with photosynthetic carbon assimilation. Trends Plant Sci **8**: 546–553

Rautengarten C, Ebert B, Liu L, Stonebloom S, Smith-Moritz AM, Pauly M, Orellana A, Scheller HV, Heazlewood JL (2016) The Arabidopsis Golgi-localized GDP-L-fucose transporter is required for plant development. Nat Commun **7**: 12119

Rawsthorne S, Hylton CM (1991) The relationship between the post-illumination CO_2 burst and glycine metabolism in leaves of C_3 and C_3-C_4 intermediate species of Moricandia. Planta **186**: 122–126

Sabar M, Balk J, Leaver CJ (2005) Histochemical staining and quantification of plant mitochondrial respiratory chain complexes using blue-native polyacrylamide gel electrophoresis. Plant J **44**: 893–901

Scheibe R (2004) Malate valves to balance cellular energy supply. Physiol Plant **120**: 21–26

Schwacke R, Schneider A, van der Graaff E, Fischer K, Catoni E, Desimone M, Frommer WB, Flügge U-I, Kunze R (2003) ARAMEMNON, a novel database for Arabidopsis integral membrane proteins. Plant Physiol **131**: 16–26

Schwender J, Shachar-Hill Y, Ohlrogge JB (2006) Mitochondrial metabolism in developing embryos of *Brassica napus*. J Biol Chem **281**: 34040–34047

Selinski J, Scheibe R (2019) Malate valves: old shuttles with new perspectives. Plant Biol **21**: 21–30

Senkler J, Senkler M, Eubel H, Hildebrandt T, Lengwenus C, Schertl P, Schwarzländer M, Wagner S, Wittig I, Braun H-P (2017) The mitochondrial complexome of *Arabidopsis thaliana*. Plant J **89**: 1079–1092

Sienkiewicz-Porzucek A, Nunes-Nesi A, Sulpice R, Lisec J, Centeno DC, Carillo P, Leisse A, Urbanczyk-Wochniak E, Fernie AR (2008) Mild reductions in mitochondrial citrate synthase activity result in a compromised nitrate assimilation and reduced leaf pigmentation but have no effect on photosynthetic performance or growth. Plant Physiol **147**: 115–127

Smith SM, Fulton DC, Chia T, Thorneycroft D, Chapple A, Dunstan H, Hylton C, Zeeman SC, Smith AM (2004) Diurnal changes in the transcriptome encoding enzymes of starch metabolism provide evidence for both transcriptional and posttranscriptional regulation of starch metabolism in Arabidopsis leaves. Plant Physiol **136**: 2687–2699

Steinbeck J, Fuchs P, Negroni YL, Elsässer M, Lichtenauer S, Stockdreher Y, Feitosa-Araujo E, Kroll JB, Niemeier J-O, Humberg C, et al. (2020). *In vivo* $NADH/NAD^+$ biosensing reveals the dynamics of cytosolic redox metabolism in plants. Plant Cell **32**: 3324–3345

Sweetlove LJ, Taylor NL, Leaver CJ (2007) Isolation of intact, functional mitochondria from the model plant *Arabidopsis thaliana*. In D Leister, JM Herrmann, eds, Mitochondria: Practical Protocols. Humana Press, Totowa, NJ, pp 125–136

Sweetlove LJ, Beard KF, Nunes-Nesi A, Fernie AR, Ratcliffe RG (2010) Not just a circle: flux modes in the plant TCA cycle. Trends Plant Sci **15**: 462–470

Taylor NL, Fenske R, Castleden I, Tomaz T, Nelson CJ, Millar AH (2014) Selected reaction monitoring to determine protein abundance in Arabidopsis using the Arabidopsis proteotypic predictor. Plant Physiol 164: 525–536

Tcherkez G, Cornic G, Bligny R, Gout E, Ghashghaie J (2005) In vivo respiratory metabolism of illuminated leaves. Plant Physiol 138: 1596–1606

Tcherkez G, Mahé A, Gauthier P, Mauve C, Gout E, Bligny R, Cornic G, Hodges M (2009) In folio respiratory fluxomics revealed by ^{13}C isotopic labeling and H/D isotope effects highlight the noncyclic nature of the tricarboxylic acid "cycle" in illuminated leaves. Plant Physiol 151: 620–630

Teschner J, Lachmann N, Schulze J, Geisler M, Selbach K, Santamaria-Araujo J, Balk J, Mendel RR, Bittner F (2010) A novel role for Arabidopsis mitochondrial ABC transporter ATM3 in molybdenum cofactor biosynthesis. Plant Cell 22: 468–480

Toka I, Planchais S, Cabassa C, Justin A-M, De Vos D, Richard L, Savouré A, Carol P (2010) Mutations in the hyperosmotic stress-responsive mitochondrial BASIC AMINO ACID CARRIER2 enhance proline accumulation in Arabidopsis. Plant Physiol 152: 1851–1862

Tomaz T, Bagard M, Pracharoenwattana I, Lindén P, Lee CP, Carroll AJ, Ströher E, Smith SM, Gardeström P, Millar AH (2010) Mitochondrial malate dehydrogenase lowers leaf respiration and alters photorespiration and plant growth in Arabidopsis. Plant Physiol 154: 1143–1157

Tovar-Méndez A, Miernyk JA, Randall DD (2003) Regulation of pyruvate dehydrogenase complex activity in plant cells. Eur J Biochem 270: 1043–1049

Tronconi MA, Fahnenstich H, Gerrard Weehler MC, Andreo CS, Flügge U-I, Drincovich MF, Maurino VG (2008) Arabidopsis NAD-malic enzyme functions as a homodimer and heterodimer and has a major impact on nocturnal metabolism. Plant Physiol 146: 1540–1552

Van Aken O, Zhang B, Carrie C, Uggalla V, Paynter E, Giraud E, Whelan J (2009) Defining the mitochondrial stress response in Arabidopsis thaliana. Mol Plant 2: 1310–1324

Van Aken O, De Clercq I, Ivanova A, Law SR, Van Breusegem F, Millar AH, Whelan J (2016) Mitochondrial and chloroplast stress responses are modulated in distinct touch and chemical inhibition phases. Plant Physiol 171: 2150–2165

van der Graaff E, Schwacke R, Schneider A, Desimone M, Flügge U-I, Kunze R (2006) Transcription analysis of Arabidopsis membrane transporters and hormone pathways during developmental and induced leaf senescence. Plant Physiol 141: 776–792

Wagner S, Nietzel T, Aller I, Costa A, Fricker MD, Meyer AJ, Schwarzländer M (2015) Analysis of plant mitochondrial function using fluorescent protein sensors. In J Whelan, MW Murcha, eds, Plant Mitochondria: Methods and Protocols. Springer New York, New York, pp 241–252

Winter H, Robinson DG, Heldt HW (1994) Subcellular volumes and metabolite concentrations in spinach leaves. Planta 193: 530–535

Wiskich J (1974) Substrate transport into plant mitochondria: swelling studies. Aust J Plant Physiol 1: 177–181

Wiskich JT (1975) Phosphate-dependent substrate transport into mitochondria: oxidative studies. Plant Physiol 56: 121–125

Wiskich JT (1977) Mitochondrial metabolite transport. Annu Rev Plant Physiol 28: 45–69

Wiskich JT, Day DA (1982) Malate oxidation, rotenone-resistance, and alternative path activity in plant mitochondria. Plant Physiol 70: 959–964

Yu H, Du X, Zhang F, Zhang F, Hu Y, Liu S, Jiang X, Wang G, Liu D (2012) A mutation in the E2 subunit of the mitochondrial pyruvate dehydrogenase complex in Arabidopsis reduces plant organ size and enhances the accumulation of amino acids and intermediate products of the TCA Cycle. Planta 236: 387–399

Zhang X, Henriques R, Lin S-S, Niu Q-W, Chua N-H (2006) Agrobacterium-mediated transformation of Arabidopsis thaliana using the floral dip method. Nat Protoc 1: 641–646

Zhao Y, Yu H, Zhou J-M, Smith SM, Li J (2020) Malate circulation: linking chloroplast metabolism to mitochondrial ROS. Trends Plant Sci 25: 446–454